90

112 N91-22989

Free Convection in the Martian Atmosphere; G.D.Clow (USGS, MS946, Menlo Park, CA 94025) and R.M.Haberle (NASA/Ames, Moffett Field, CA 94035)

We investigate the "free convective" regime for the martian atmospheric boundary layer (ABL). This state occurs when the mean windspeed at the top of the ABL drops below some critical value U_c and positive buoyant forces are present. Such forces can arise either from vertical temperature or water vapor gradients across the atmospheric surface layer. During free convection, buoyant forces drive narrow plumes that ascend to the inversion height with a return circulation consisting of broad slower-moving downdraughts. Horizontal pressure, temperature, windspeed, and water vapor fluctuations resulting from this circulation pattern can be quite large adjacent to the ground (within the surface layer). These local turbulent fluctuations cause non-zero mean surface stresses, sensible heat fluxes, and latent heat fluxes, even when the mean regional windspeed is zero. Although motions above the surface layer are insensitive to the nature of the surface, the sensible and latent heat fluxes are primarily controlled by processes within the interfacial sublayer immediately adjacent to the ground during free convection. Thus the distinction between aerodynamically smooth and rough airflow within the interfacial sublayer is more important than for the more typical situation where the mean regional windspeed is greater than U_c. Buoyant forces associated with water vapor gradients are particularly large on Mars at low pressures ($P<30$ mb) and high temperatures ($T>250$ K) when the surface's relative humidity is 100%, enhancing the likelihood of free convection under these conditions. On this basis, Ingersol [1] postulated the evaporative heat losses from an icy surface on Mars at 273 K and current pressures would exceed the available net radiative flux at the surface, thus prohibiting ice from melting at low atmospheric pressures.

Recently, Schumann [2] has developed equations describing the horizontal fluctuations and mean vertical gradients occurring during free convection. However, his model is limited to the case where free convection is driven solely by thermal buoyancy and the surface is aerodynamically rough. Within these restrictions, model results compare very well with those of a detailed large-eddy simulation (LES) which in turn generally agree with available atmospheric observations [3]. Despite large horizontal wind velocities associated with the updraughts, the LES demonstrates that the time-derivatives for horizontal motion in the surface layer are small, validating the use of Monin-Obukhov theory in the model.

We have generalized Schumann's model to include convection driven by water vapor gradients and to include the effects of circulation above both aerodynamically smooth and rough surfaces. Applying the model to Mars, we find that nearly all the resistance to sensible and latent heat transfer in the ABL occurs within the thin interfacial sublayer at the surface. Free convection is found to readily occur at low pressures and high temperatures when surface ice is present. At 7 mb, the ABL should freely convect whenever the mean windspeed at the top of the surface layer drops below about 2.5 m s^{-1} and surface temperatures exceed 250 K. Mean horizontal fluctuations within the surface layer are found to be as high as 3 m s^{-1} for windspeed, 0.5 K for temperature, and 10^{-4} kg m^{-3} for water vapor density. Airflow over surfaces similar to the Antarctic Polar Plateau (surface roughness length z_0 approx. 0.03 cm) is found to be aerodynamically smooth on Mars during free convection for all pressures between 6 and 1000 mb while surfaces with $z_0 = 1$ cm are aerodynamically rough over this pressure range.

Free convective latent-heat fluxes are of particular interest because they establish the *minimum* evaporative heat losses that will occur for an icy surface at a given temperature. Fig.1 shows the predicted latent heat fluxes during free convection for the limiting case where the ABL is isothermal and the surface temperature is 273 K. For a surface resembling average terrestrial polar snows (curve A), our predicted fluxes are a factor of 4 smaller than those given by Eq.(1) of Ingersol [1], making it proportionally easier to melt ice on Mars. Fig.2 shows the albedo required for the net radiative flux at the surface to just balance the predicted latent heat losses at 273 K at the time of maximum incoming solar radiation. The lowest albedo that can be achieved for martian ice surfaces is about 0.2 [4]. Hence, atmospheric pressures need to be at least 100 mb at the poles and about 6 mb at the equator before ice can melt under the best of conditions.

References: [1] Ingersol,A.P. (1970) **Science, 168,** 972-973; [2] Schumann,U. (1988) **Boundary-Layer Meteorol., 44,** 311-326; [3] Schmidt,H. and U.Schumann (1989) **J.Fluid Mech., 200,** 511-562; [4] Clow,G.D. (1987) **Icarus, 72,** 95-127.

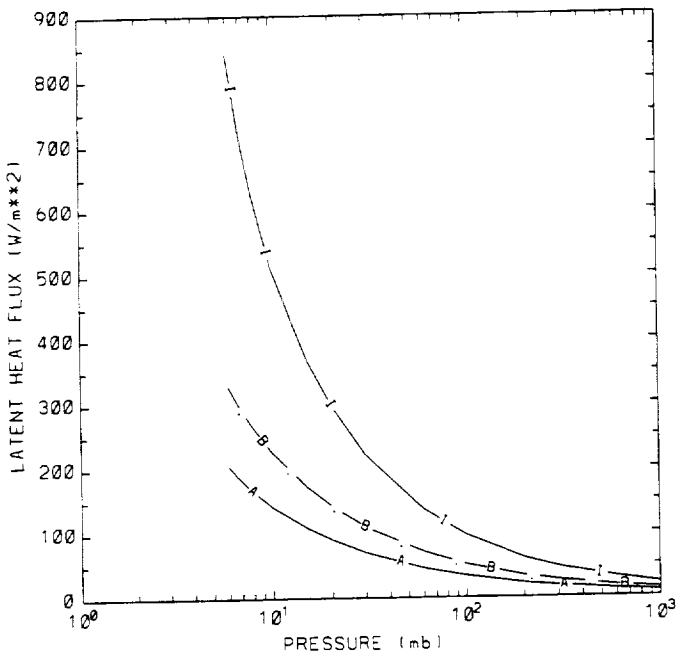

Fig.1: Predicted latent heat fluxes at 273 K for a surface with $z_0 = 0.03$ cm (curve A) and $z_0 = 1$ cm (curve B). Shown for comparison are the free convection predictions of Ingersol [1], (curve I).

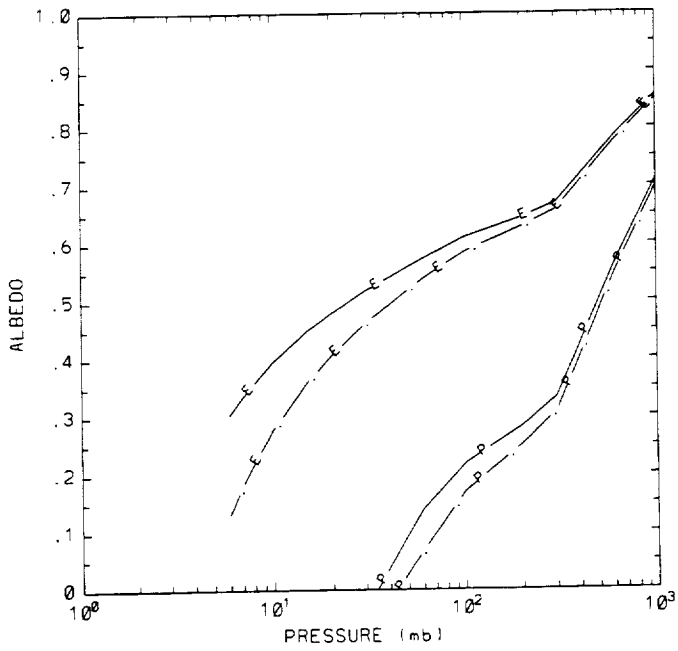

Fig.2: Highest albedos for which ice can melt under optimal conditions in the equatorial regions (curves E) and the polar regions (curves P). Solid lines refer to aerodynamically smooth surfaces while dashed lines are for aerodynamically rough surfaces.

THERMOKARSTIC DEPRESSIONS AT THE MOUTH OF ELYSIUM CHANNELS (MARS): NEW EVIDENCE FOR THE PRESENCE OF MASSIVE ICY BEDS.

F.M. COSTARD, Laboratoire de Géographie Physique URA DO141, CNRS, 92195 Meudon Cédex, France.

The analysis of very high resolution Viking pictures (12 m/pixel) in Utopia Planitia indicates a concentration of thousand of depressions at the mouth of Elysium channels. Their spatial distribution concern an area of 220.000 km² between 237°W to 271°W and 41°N to 50°N. These depressions are 130 m to 3 km in length and 20 m to 45 m in depth and occupy a regional depression whose floor altitud is -2 km (fig. 1). The occurrence in the same area of very high density fluidized ejecta craters implies the presence of a continuous and subsurface ground-ice (1) probably in thick sediment deposits (2, 3, 4). The purpose of this study is to compare these depressions with thermokarstic features of Yakutia (Siberia). An eolian origin would produce elongated shapes and not circular depressions as they are actually observed. A kettle hypothesis is also unlikely because of the lack of moraine like ridges in the vicinity.

a) Circular depressions:

These depressions are the most numerous. They are similar in size and form to thermokarstic depressions (alases) of terrestrial Arctic regions (fig. 2). In Yakutia, alases are well developped in presence of massive icy beds which can be as much as 2 km in length and 40 m in thickness (5). On Mars, the occurrence of alases implies a near surface ground-ice which contains massive icy beds (6). A change in the thermal balance of ground-ice, during a warmer climate or a geothermal heating, would produced melting or sublimation of the ice with an extensive alas development.

b) Annular depressions:

In the same area, a few tens of fluidized ejecta craters exhibit an annular moat at the edge of the ejecta blanket. The complete evolution of these annular moats since their formations until their complete developments will be retraced. A thermokarstic origin is also proposed. Just after the formation of the ejecta lobe, a post-deposition fluid flow produced a concentration of volatiles in the edge of the ejecta lobe (fig. 3-B). Such a mechanism is attested by the occurence of channels on some ejecta blankets (fig. 3-A) as advocated by Mouginis-Mark (7). Under the cold climate conditions of planet Mars, freezing of water involved a modification of the porous structure of ground-ice. Its subsequent melting produced individual alases (fig. 3-C) where slope retreats resulted in a progressive widening around the ejecta lobe (fig. 3-D, E). Finally their intersection produces a complete annular moat (fig. 3-F).

c) Stratified deposits.

As advocated by Zimbelman et al. (8), Utopia Planitia seems to be covered by a stratified deposit. The deepest alases reveal an horizontal deposit with three or four layers. In many places, the layers exhibit a trangressive overlap over a distance of 2 km (fig. 4). Such observations involve a stratification of sediments during different episods of channeling and sedimentation with a kind of cross-bedding. Such an apparent stratification on the alas slopes is not consistent with a collapse process. It is supposed that an aeolian erosional process might reveals locally that stratification after the thermokarst episod. The reduced energy regime at the mouth of Elysium channels may have involved a preferential accumulation of fine grained deposit easily removable by an eolian process. Under a cold climate condition, such sediments might have contained considerable amounts of ice (massive icy beds, ice segregations) which favored intense development of thermokarst features.

Conclusion: The occurence of such circular and annular thermokarstic depressions at the mouth of outflow channels supports the presence of a volatile-rich fluvial sediments which contain major amount of massive icy beds.

This work was supported by INSU (ATP de Planétologie) n°876714.

References: (1) Costard, F.M. (1989): Earth, Moon and Planets, 45: 265-290. (2) Lucchitta, B.K., Ferqusson, H.M. and Summers, C. (1986): Proc. 17th Lunar and Planet. Sci. Conf., J.G.R. pp. E166-E174. (3) Mc Gill, G.E. (1985): Lunar and Planet. Sci. Conf. pp. 534-535. (4) Jons, H.P. (1985): Proc Lunar and Planet Sci. Conf., 414-415. (5) Mackay, J.R. (1973): Permafrost Conf., pp.223-228. (6) Costard, F.M. (1988): Lunar and Planet. Sci. Conf. pp. 211-212. (7) Mouginis-Mark, P.J. (1987): Icarus, 71:268-286. (8) Zimbelman, J.R., S.H. Clifford and S.H. William (1989): Proc. 19th Lunar and Planet. Sci. Conf., J.G.R. pp. 397-407.

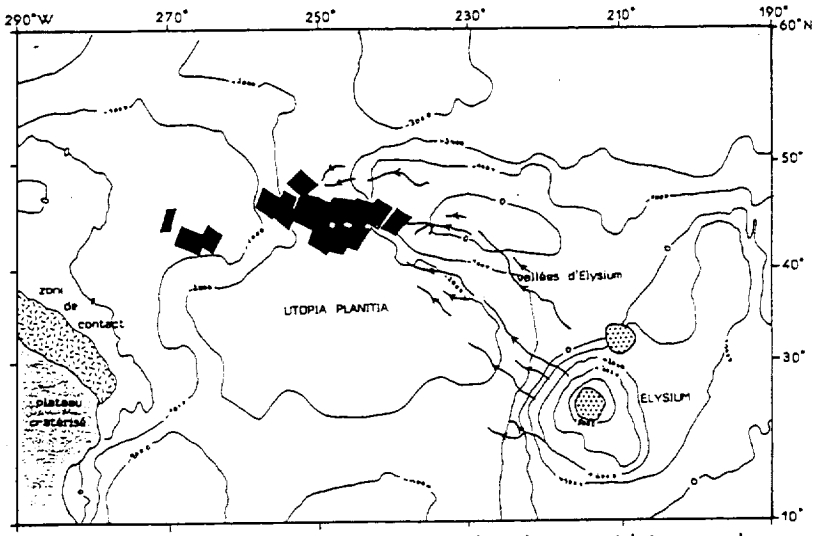

Fig. 1: Location of high resolution Viking images which comprise alas depressions (solid black). Note their association with Elysium channels (solid lines with arrows).

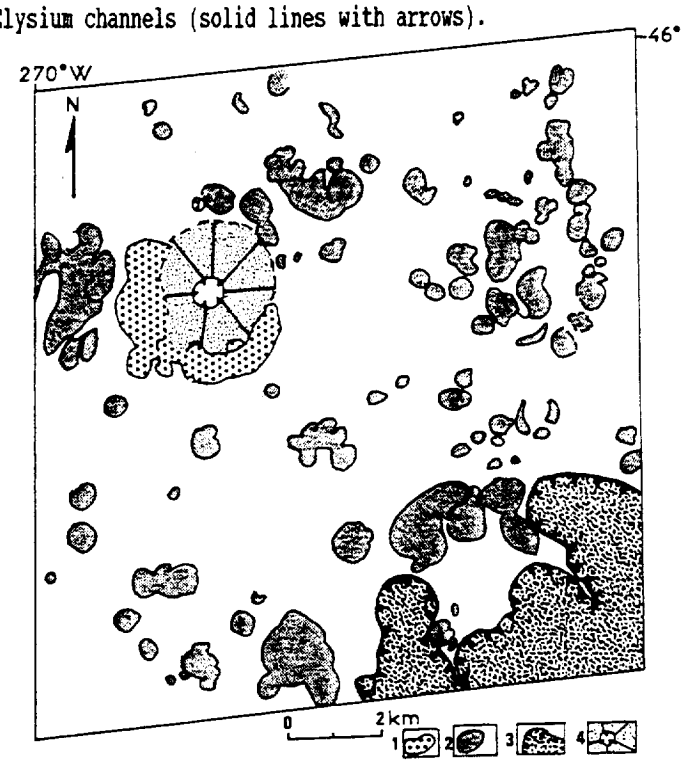

Fig. 2: Alas depressions in Utopia Planitia at the mouth of Elysium channels. (1): annular moat, (2): circular depression, (3): large thermokarst depression, (4): fluidized ejecta crater.

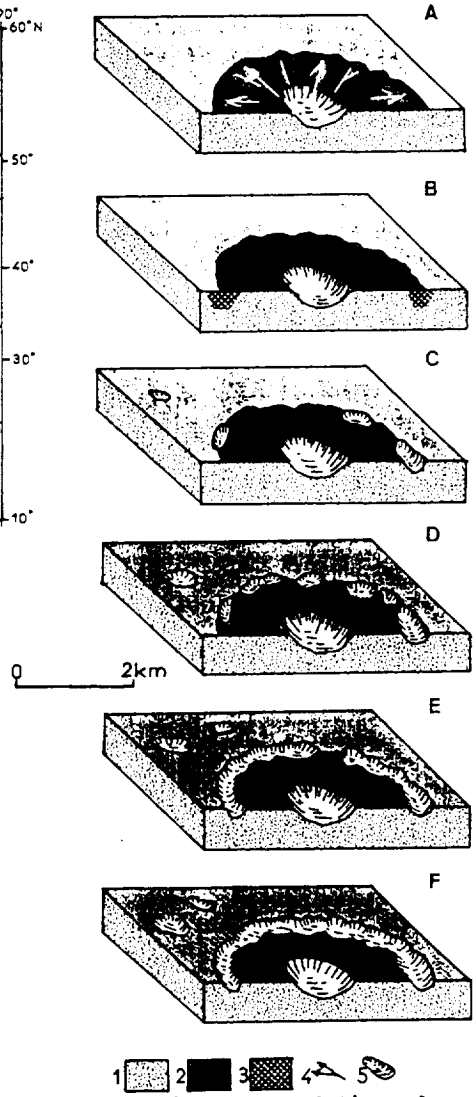

Fig. 3: Formation and evolution of an annular moat around a fluidized ejecta crater. 1: ground-ice; 2: ejecta blanket; 3: volatile concentration; 4: channels; 5: alas.

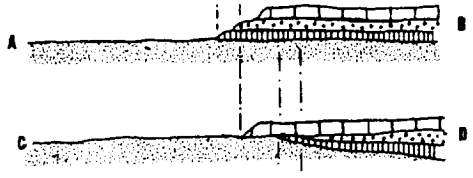

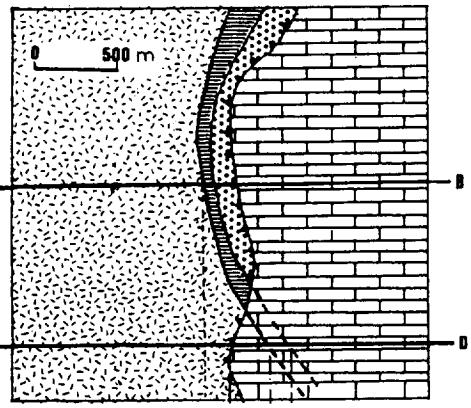

Fig. 4: Map showing a transgressive overlap within stratified deposits of a thermokarst collapse.

RATIONALE FOR A MARS ROVER/SAMPLE RETURN MISSION TO CHRYSE PLANITIA AND THE VIKING 1 LANDER; Robert A. Craddock, Center for Earth and Planetary Studies, National Air and Space Museum, Smithsonian Institution, Washington, DC 20560

As a precursor to a sample return mission and/or manned mission to Mars, landing sites that are both safe and scientifically interesting must be determined. Potential sites could ultimately affect spacecraft design and development and determine the range of scientific objectives possible. The earlier potential sites are selected, the more cost and time efficient mission planning and operations will be. However, Mars has as much land surface area as the continental crust of the Earth and exhibits a wide variety of geologic processes and features thus making site selection an arduous task.

So why go back to Chryse Planitia, an area previously explored by the Viking 1 Lander? One of the best reasons is that we have already been there. Viking 1 landed successfully, proving that it is safe and providing us with valuable ground-truth observations of the martian surface. For example, Viking Lander 1 data have provided information useful in determing the physical properties of the martian surface materials [e.g., 1]. Observations such as these will undoubtingly be incorporated into any future spacecraft design--no matter where the designated landing site is located. In addition, Chryse Planitia still represents one of the lowest spots on the surface of Mars (>2 km below mean Mars datum; 2), providing more atmosphere to slow down a landing vehicle. Its equatorial location (~20° N lat.) allows contact with both polar and equatorial orbiting spacecraft along with direct line-of-site communications with the Earth, an added bonus when sending commands to a moving vehicle. The extensive photographic coverage of Chryse Planitia by the Viking Orbiters and Earth-based radar observations have provided 100 m resolution topography in the vicinity of the Viking 1 Lander [e.g., 2]. Analysis of these data and lander photographs indicate that Chryse Planitia may be unique in that features >50 km away from the lander (such as the rims of Lexington and Yorktown craters) are visible over the horizon [3]. This information could potentially provide a valuable check for determining the location of the spacecraft on the surface and aid in roving vehicle navigation.

Ideally a landing site should include access to as many different geologic units as possible. In addition to the materials debouched into the Chryse basin by the large martian channel complex [e.g., 4], the Hesperian age ridged plains covering much of region [5] may represent the single most important geologic unit needed for age-dating materials on Mars. Composing ~3% of the total Mars surface area [6], the ridged plains are fairly widespread in comparison to other geologic units and, more importantly, are the Hesperian epoch referent [7]. Because the Hesperian epoch represents the interval of time immediately following the period of heavy bombardment (~3.8 Ga; 8), an absolute age determined from a ridged plain sample would allow estimates of the post-heavy bombardment impact flux on Mars to be calibrated. It may then be possible to determine the absolute ages of every younger geologic unit on Mars based on crater statistics. In addition, materials washed down from the highlands may be present in the vicinity of Lander 1. Although the absolute ages of these materials almost certainly correspond to the period of heavy bombardment, analysis of their composition could provide some insight into the early geologic history of Mars. Also the distribution of the materials in Chyrse Planitia as determined by a manned or unmanned traverse may be indicative

of the channel formation mechanism. For example, catastrophic flooding would lead to a Bouma sequence deposit in the Chryse basin [9]; in liquefaction, an accretionary lobe in the debouching area results in larger particles dropping out first with smaller particles being transported greater distances [10].

Because of the likelihood of running water debouching into Chyrse Planitia in the past, the Viking 1 landing site was considered an ideal place to look for complex organic molecules [11]. Although the Viking biological experiments did not identify the presence of organic life [12], controversy still exists as to the meaning of the Label Release Experiment [13]. Knowing the position of Viking 1 on the surface to within 50 m [14], it would be possible to navigate to the landing site and obtain the same soil samples investigated by the lander. Rocks seen in lander images could also be returned to Earth, answering questions concerning their compositional and erosional properties. A piece or pieces of Lander 1 itself could be obtained! Especially easy to recover is the small latch pin released when the lander sampler shroud was jettisoned. This 8.2 cm long and 0.6 cm diameter pin fell within 1 m of the lander, weighs 11.3 g, and has been exposed to the martian environment for a known period of time. No special tools would be needed to obtain the latch pin, and analysis upon return to earth would provide erosion rates and other information useful in understanding geologic processes. In situ erosional analysis of Lander 1 itself could also have implications on the development of future martian spacecraft materials. In addition, it may be possible to navigate from the lander to the crater caused by the jettisoned Viking aeroshell. Ejecta from this fresh crater would represent Chryse stratigraphy at depth, providing a possible alternative if a drill sample is determined impractical for the early sample return missions. Yorktown, a 7.9-km-diameter "rampart" [15] or "fluidized ejecta" crater [16], is ~45 km northwest of the Viking 1 landing site as well. Samples of the ejecta from Yorktown could determine how much volatile material is involved in rampart crater formation [e.g., 15], if any at all [17]. Following the Xanthe Dorsa ridge north for ~34 km from the Viking 1 Lander to the crater San Juan, Yorktown is ~22 km to the west. An active seismic or sounder experiment operated along the Xanthe Dorsa ridge traverse could provide clues to the ridge structure and the underlying Chryse basin stratigraphy.

REFERENCES: [1] Moore, H.J., et al., U.S.G.S. Prof. Paper 1389, 222 pp., U.S. Government Printing Office, Washington, 1987. [2] U.S.G.S. Misc. Invest. Series Map I-1059, Controlled mosaic of the Yorktown region of Mars, U.S. Geol. Surv., Denver, CO, 1977. [3] Craddock, R.A. and J.R. Zimbleman, Lunar Planet. Sci., XX, 193-194, 1989. [4] Greeley, R., et al., J. Geophys. Res., 82, 4093-4109, 1977. [5] Scott, D.H. and K.L. Tanaka, U.S. Geol. Surv. Misc. Invest. Series Map I-1802A, U.S. Geol. Surv., Denver, CO, 1986. [6] Watters, T.R., Abstracts for the MEVIV-LPI Workshop: Early Tectonic and Volcanic Evolution of Mars, 63-65, 1988. [7] Tanaka, K.L., J. Geophys. Res., 91, E139-E158, 1986. [8] Hartmann, W.K., et al., In Basaltic Volcanism on the Terrestrial Planets, Pergamon, New York, 1981. [9] Komar, P.D., Icarus, 42, 317-329, 1980. [10] Nummedal, D., and D.B. Prior, Icarus, 45, 77-86, 1981. [11] Masursky, H. and N.L. Crabill, Science, 193, 809-812, 1976. [12] Klein, H.P., J. Geophys. Res., 82, 4677-4680, 1977. [13] Levin, G.V. and P.A. Straat, J. Geophys. Res., 82, 4663-4667, 1977. [14] Morris, E.C. and K.L. Jones, Icarus, 44, 217-222, 1980. [15] Carr, M.H., et al., J. Geophys. Res., 82, 4055-4066, 1977. [16] Mouginis-Mark, P.J., J. Geophys. Res., 84, 8011-8022, 1979. [17] Schultz, R.A. and D.E. Gault, Third International Colloquium on Mars, 226-228, 1981.

EVIDENCE FOR WIDESPREAD RESURFACING IN THE MARTIAN HIGHLANDS;
Robert A. Craddock and Ted A. Maxwell, Center for Earth and Planetary Studies, National Air and Space Museum, Smithsonian Institution, Washington, DC 20560

The southern cratered highlands of Mars contain a large population of flat-floored, rimless craters which occur on a variety of Noachian geologic materials. Previously these craters have been interpreted to have formed by aeolian mantling [1] or flood volcanism [2]; however, neither of these geologic processes accurately explains the observed morphology or the crater statistics. Determining the distribution of the flat-floored, rimless craters, the timing of the process responsible for their formation, and the actual process involved in their formation is important for understanding the geomorphic evolution of most of the southern cratered hemisphere of Mars. Our initial investigation concentrated on the analysis of the Amenthes and Tyrrhena regions near the dichotomy boundary [3,4,5]. Currently we have begun investigations into other areas including Mare Australe, Eridania, Arabia, Noachis, and Memnonia.

The geologic analysis of these regions was based on the published 1:15M geologic maps of Mars and was limited to two materials: the Noachian cratered unit (Npl_1; 6) and the Noachian dissected unit (Npld; 6). Although flat-floored, rimless craters occur on other Noachian geologic materials as well, the interpretations of these units [7,8,9] includes resurfacing by processes we feel are separable from a larger, more extensive process. The Noachian cratered unit (Npl_1) and the Noachian dissected unit (Npld) are distinguished by the absence or presence of ancient valley networks (i.e., runoff channels), respectively [6]. Together these units make up a bulk (~70%) of the surface area of the southern cratered hemisphere.

The termination of the resurfacing event represented by the cumulative size-frequency curves of superposed, fresh craters was not a catastrophic, global event (Fig. 1). Resurfacing ceased during the late Noachian to early Hesperian in the regions analyzed. In general, resurfacing ceased in the Npld materials later than in the Npl_1 materials, suggesting that the ancient valley networks represent the late stages or a change in the resurfacing process. These observations correlate well with other work suggesting that the ancient valley networks ceased to form by the early Hesperian [6].

A proposed mechanism responsible for martian highland resurfacing must be able to explain not only the morphology of the flat-floored, rimless, craters, but also the timing of the process between regions and the bendover in crater size-frequency distribution curves of highland materials [e.g., 5] as well. Although a bulk of the cratered highlands may be composed of volcanics [e.g., 10], volcanism does not produce flat-floored, rimless craters except in very rare circumstances. Aeolian erosion/deposition is also a very active process on Mars as evidenced by the seasonal dust storms and a variety of landforms [e.g., 11]; however, unlike what has been suggested by Wilhelms and Baldwin (1) aeolian fallout would not only be deposited up to the rim crest of craters but <u>on</u> the rims of craters as well. The result is not to produce a flat-floored, rimless crater, but to subdue the morphology of the crater. Volcanic and aeolian resurfacing do not produce a bendover in the cumulative size-frequency curves either. In both processes a crater is either buried, or it is not, in which case it is still counted. We propose a fluvial process capable of eroding the rims of the craters primarily from the outside, thus reducing the apparent diameter of the craters. The eroded material is

redistributed, inundating the smaller craters before they are eroded completely. Such a complicated process not only explains the morphology of the flat-floored, rimless craters, but also the bendover in the cumulative size-frequency curves and potentially the timing of the process between regions.

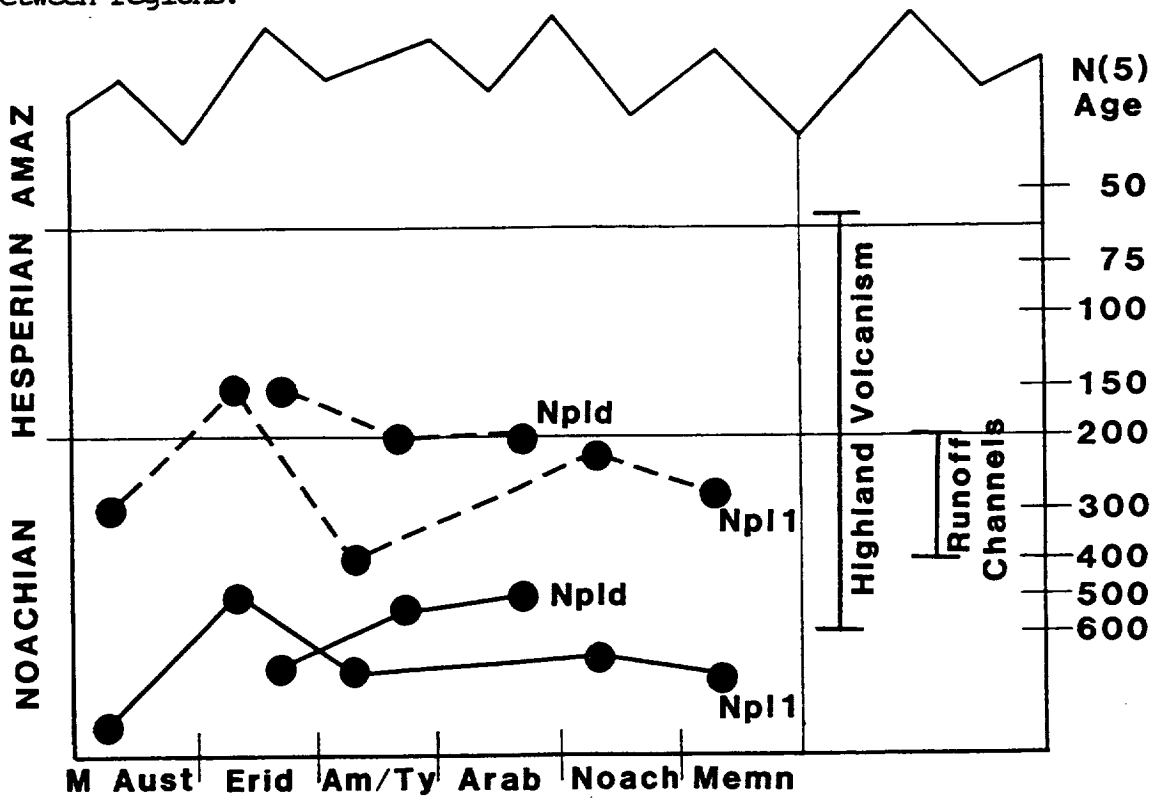

Figure 1. Timing of resurfacing in the areas mentioned in text. N(5) ages represent the number of craters >5-km-diameter per million square kilometers. Solid lines represent age of material based on all craters. Dashed lines represent termination of resurfacing event based on fresh, superposed craters.

REFERENCES: [1] Wilhelms, D.E. and R.J. Baldwin, Proc. Luanr Planet. Sci., 19th, 355-365, 1989. [2] Hartmann, W.K. et al., In Basaltic Volcanism on the Terrestrial Planets, Chap. 8, pp. 1049-1127, Pergamon, New York, 1981. [3] Craddock, R.A. and T.A. Maxwell, Lunar Planet. Sci., 20, 191-192, 1989. [4] Maxwell, T.A. and R.A. Craddock, Lunar Planet. Sci., 20, 646-647, 1989. [5] Craddock, R.A. and T.A. Maxwell, Resurfacing of the martian highlands in the Amenthes and Tyrrhena region, J. Geophys. Res., in review. [6] Tanaka, K.L., Proc. Lunar Planet. Sci. Conf., 17th, in J. Geophys. Res., 91, E139-E158, 1986. [7] Scott, D.H., and K.L. Tanaka, Geologic map of the western equatorial region of Mars, 1:15M scale, U.S.G.S. Map I-1802-A, 1986. [8] Greeley, R. and J.E. Guest, Geologic map of the eastern equatorial region of Mars, 1:15M scale, U.S.G.S Map I-1802-B, 1987. [9] Tanaka, K.L. and D.H. Scott, Geologic map of the polar regions of Mars, 1:15M scale, U.S.G.S. Map I-1802-C, 1987. [10] Greeley, R. and P.D. Spudis, Rev. Geophys. Space Phys., 19, 13-41, 1981. [11] Thomas, P., J. Geophys. Res., 87, 9999-10,008, 1982.

GEOLOGIC HISTORY OF THE SOUTHERN REACHES OF MANGALA VALLES, MARS; Robert A. Craddock[1], James R. Zimbelman[1], and Ronald Greeley[2], [1]Center for Earth and Planetary Studies, National Air and Space Museum, Smithsonian Institution, Washington, DC 20560, [2]Department of Geology, Arizona State University, Tempe, AZ 85287

Mangala Valles is unique in that unlike the other large martian outflow channels it does not originate from chaotic terrain, nor does it debouch into a basin such as Chryse Planitia. Deriving the geologic history of Mangala Valles is important for determining the cause of postulated subsurface volatile release and understanding the reasons for martian channel formation. Analysis of Mariner and Viking images and Earth-based radar topography in the Mangala Valles/Memnonia region of Mars as part of the Mars Geologic Mapping program has identified several important steps in the history of Mangala Valles.

As evidenced by the orientation of Imbrium Sculpture-like groves and the circular occurrence of massifs and faults, a 6400-km-diameter, early Noachian basin has been identified in the center of Daedalia Planum [1], confirming observations made by Earth-based radar data [2]. In the Memnonia region, the Daedalia basin caused an eastern slope to the topography and uplifted an arc of highland material, which define an inner ring ("m/r" in Fig. 1). Subsequent radial faulting composing the Memnonia Fossae and associated with the formation of the Tharsis Montes [3] intersected this inner ring, possibly forming conduits for the migration of subsurface volcanic material. We suggest that some the volcanic material extruded to the surface and flowed along the eastern side of the massif ("lf" in Fig. 1). Although the vent for these materials is probably buried, a possible source is the circular depression located along the margin of the ring massif (Fig. 2; "o" in Fig. 1). With time the volcanic heat source also melted a sufficient portion of the volatile resevoir frozen in the eastward sloping highlands, thus allowing a hydrostatic head to develope. Volatiles were released along the cracked tips of en echelon Memnonia Fossae at -18.5°, 149.4° ("x" in Fig. 1). Evacuation of the volcanic material may have also caused rotation of part of the massif (see dashed block in Fig. 1) and induced release of the volatiles under a hydrostatic head at the present source area of Mangala Valles.

Initial flooding associated with the formation of Mangala Valles seems to have been widespread during the late Hesperian. Volatiles partially filled the large crater cross-cut by the source graben [4] and were ponded in the depression adjacent to the massif (Fig. 2). The volatiles ponded by the massif depression may have percolated through the material underlying the lava flow ("lf"), causing sapping and back-wasting along the flow margin (arrows in Fig. 1). Radar-derived topography indicates that southern Mangala Valles has an average gradient of .001 [5], which is comparable to active rivers at similar distances from their sources [6]. This suggests that fluvial activity at Mangala Valles may have been sufficiently longlived to produce a graded profile, while becoming more localized with time. Analysis of available photographs and crater size-frequency data from the Daedalia Planum plains east of the massif suggest that Amazonian volcanic material may have extruded through an extension of the Mangala Valles source graben ("lf_2" in Fig. 1). These materials may represent the termination of volcanic activity in the area and associated channel flooding since they appear to post-date the channel materials [7].

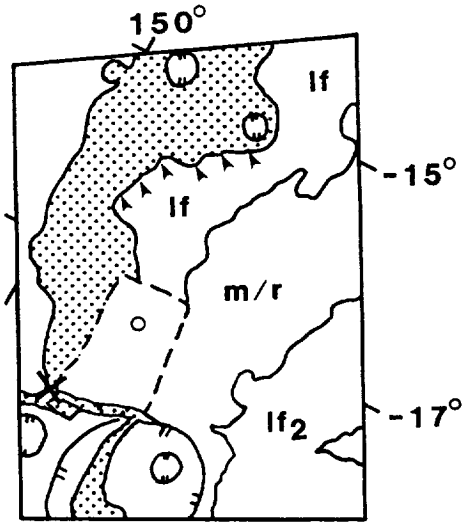

Figure 1 (left). Schematic diagram of features visible in Fig. 2. Stippled pattern represents Mangala Valles channel materials.

Figure 2 (below). Stereoscopic pair showing features discussed in text. Viking orbiter frames 637A82 (left) and 639A11 (right). (Stereoscopic viewers can be found in NASA SP-441 or NASA SP-445.)

ORIGINAL PAGE
BLACK AND WHITE PHOTOGRAPH

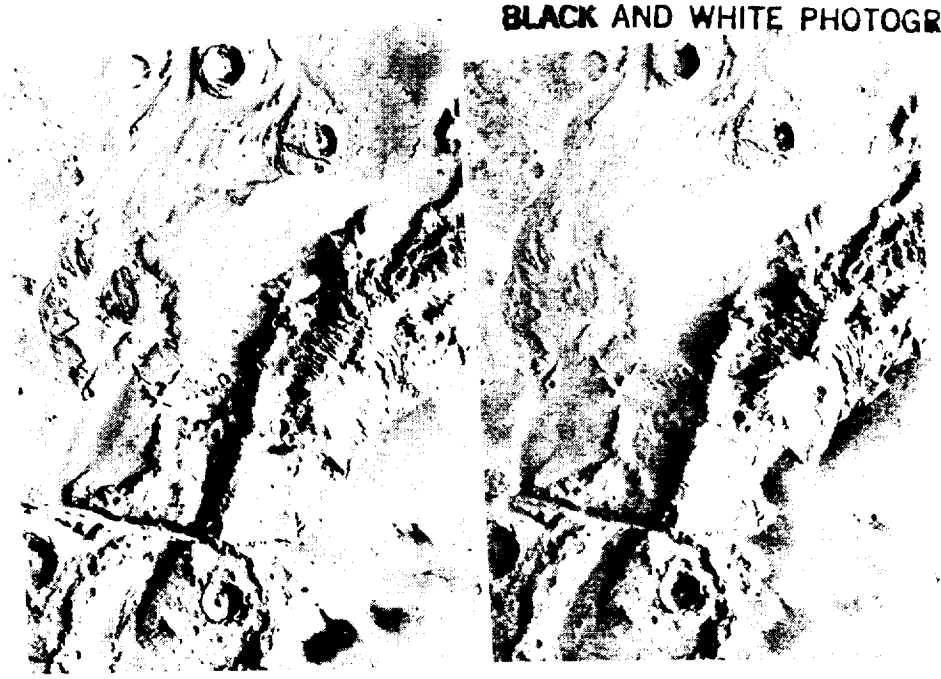

REFERENCES: [1] Craddock, R.A. et al., Evidence for an ancient impact basin in Daedalia Planum, Mars, J. Geophys. Res., in review. [2] Plescia, J.B. et al., Lunar Planet Sci., 11, 891-893, 1980. [3] Plescia, J.B. and R.S. Saunders, J. Geophys. Res., 87, 9775-9792, 1982. [4] Pfau, C.E. and S.R. Saunders, NASA TM-86247, 152-155, 1984. [5] Zimbelman, J.R., Lunar Planet Sci., 20, 1239- 1240, 1989. [6] Leopold, L.B. et al., Fluvial Process in Geomorphology, Freeman & Co., p. 190, 1964. [7] Greeley, R. and R.A. Craddock, Geologic Map of the Southern Mangala Valles Region of Mars, scale 1:500K, in review.

STYLES OF VOLCANISM, TECTONIC ASSOCIATIONS, AND EVIDENCE FOR MAGMA-WATER INTERACTIONS IN EASTERN HELLAS, MARS

David A. Crown and Ronald Greeley, Department of Geology, Arizona State University, Tempe, Arizona 85287

Four of the martian highland paterae (low-relief, areally-extensive features with central calderas and radial channels and ridges [1,2]) are associated with inferred rings of the Hellas basin [3,4] (Figure 1). Their morphometry [5] and the erosional characteristics of Tyrrhena Patera [2] have been used as evidence that they are composed of ash. Analyses of the energetics of eruption and flow processes have shown that the distribution of units at Hadriaca and Tyrrhena Paterae is consistent with an origin by the emplacement of gravity-driven pyroclastic flows and that explosive eruptions driven by magmatic volatiles or groundwater could provide sufficient energy [6-9]. The supply of groundwater for hydromagmatic eruptions has been considered; large volumes of water could accumulate rapidly at flow rates determined for Mars [7,10-11]. The present investigation synthesizes the previous studies of Tyrrhena Patera and results of modeling martian volcanic processes with current photogeologic investigations of the Hadriaca Patera region [6,12] in order to examine the evolution of volcanism in the eastern Hellas region.

In eastern Hellas, Hadriaca and Tyrrhena Paterae are observed in association with the ridged plains of Hesperia Planum. Zones of weakness generated by the Hellas impact event may have produced conduits for the magmas forming these deposits [4]. The structure of Hellas has clearly influenced the shapes of the paterae, which are elongated downslope toward the basin, as well as the positions of the volcanic source vents. The orientations of 243 ridges have been mapped in the Hadriaca [260-275° W, 27.5-42.5° S] and Tyrrhena [247.5-265° W, 15-30° S] regions. The 219 ridges contained within volcanic units have a wide range of orientations but exhibit trends which approximate radial (NE-SW) and concentric (NW-SE) patterns to Hellas. Although orthogonal and parallel alignments between ridges and the regional slope and lava flow directions in the flank flow unit at Tyrrhena are also observed, basin-related tectonism is considered the primary factor governing ridge orientation because the regional slope is a consequence of the basin and has controlled the emplacement of the volcanic units. The NE-SW and NW-SE ridge orientations measured agree with previously documented trends for Hesperia Planum [13] and indicate the effects of the Hellas impact event over a wide region of the southern highlands and the persistence of the tectonic signature of the basin over geologic time.

Photogeologic studies indicate that Tyrrhena Patera consists of basal and summit shield units, the surfaces of which contain channels radiating from the summit caldera region [6-7,12]. Layering is observed in these units, the distal margins of which are highly dissected and form isolated erosional remnant mesas. The large flank flow unit composed of well-defined lava flow lobes and leveed channels, the first definitive evidence for effusive volcanic activity associated with the paterae, extends from near the summit of Tyrrhena for over 1000 km to the SW adjacent to Hadriaca. Hadriaca Patera also exhibits channeled flanks, although the channels are smaller and more closely spaced. Multiple layers and erosional remnants are also observed. The morphologies of these volcanoes suggest that their surfaces have been modified by fluvial erosion (sapping?), and these erosional characteristics in combination with similar morphometry to large terrestrial ash sheets [5] and the absence of primary lava flow features (except in the flank flow unit) suggest that the highland paterae are composed primarily of ash [6,7].

Cross-cutting relationships determined from geologic mapping of eastern Hellas indicate that the ridged plains of western Hesperia Planum and the flank flow unit at Tyrrhena Patera are younger than the basal and summit shield units [7,12], suggesting a transition from explosive to effusive volcanism. The erosion of the flanks of Hadriaca pre-dates the erosion of the channeled plains to the south. The erosion on the plains (presumably by runoff) and the eventual formation of the Dao Vallis outflow system continues through the formation of the flank flow. Thus, the erosional processes affecting Hadriaca and Tyrrhena Paterae and the plains were probably active, at least in some areas, after the emplacement of the flank flow. This relationship supports the interpretation of the dissected units at Hadriaca and Tyrrhena as ash rather than eroded lavas because the flank flow unit should have been subjected to similar degradational processes, at least

in the south near Hadriaca. The presence of volatile-rich surface materials in the region is strongly supported by the morphologies of the channeled plains and Dao Vallis [6,11]. In addition, debris flows and pitted plains associated with Noachian mountains near Harmahkis Vallis illustrate the influence of near-surface volatiles. The transition from explosive to effusive volcanism (from the low shields of the paterae to the flank flow unit and the ridged plains of Hesperia Planum) can be interpreted as the result of the cessation of magma-volatile interactions. Groundwater could have been concentrated by the topography of Hellas and would have moved easily in the fractured highland crust. The interpretation of the caldera-filling materials at the paterae as late-stage lavas [7] is consistent with this scenario, as the rising magma could eventually seal the conduit from further inflow by water [14]. In addition, as the volcanoes increased in size, water would tend to flow away from the structures, and even if contact occurred beneath the surface, explosive eruptions could be suppressed by the increasing weight of the volcano. Explosive eruptions at Tyrrhena would have ceased first due to its distance from Hellas.

The style of eruptive activity in eastern Hellas has implications for the general evolution of martian volcanism. If magmatic eruptions generated the pyroclastic flows forming the paterae, this suggests an evolution in magma types from Hesperian to Amazonian time, when the Tharsis and Elysium volcanics formed, and/or the existence of spatial heterogeneities in the mantle from which the magmas were derived. Hydromagmatic origins for the paterae imply an evolution from volatile-rich to volatile-poor eras in the near-surface environment of Mars, in accordance with proposed global climatic changes [15]. While the observed morphologies and the energetics of explosive eruptions are consistent with both magmatic and hydromagmatic origins of Hadriaca and Tyrrhena Paterae, consideration of the regional geologic setting supports the role of magma-volatile interactions in the volcanism of the eastern Hellas region.

References: [1] Plescia, J.B. and R.S. Saunders, 1979, *Proc. Lunar Planet. Sci. Conf., 10th,* 2841-2859. [2] Greeley, R. and P.D. Spudis, 1981, *Rev. Geophys. Space Phys., 19,* 13-41. [3] Peterson, J.E., 1978, *Proc. Lunar Planet. Sci. Conf., 9th,* 3411-3432. [4] Schultz, P.H., 1984, *Lunar Planet. Sci. Conf., XV,* 728-729. [5] Pike, R.J., 1978, *Proc. Lunar Planet. Sci. Conf., 9th,* 3239-3273. [6] Crown, D.A. and R. Greeley, 1990, in *MEVTV Workshop on the Evolution of Magma Bodies on Mars,* L.P.I., in press. [7] Greeley, R. and D.A. Crown, 1990, *J. Geophys. Res.*, in press. [8] Crown, D.A. et al., 1988, *Lunar Planet. Sci. Conf., XIX,* 229-230. [9] Crown, D.A. and R. Greeley, 1988, *LPI Technical Report 89-04,* 29-31. [10] Carr, M.H., 1979, *J. Geophys. Res., 84,* 2995-3007. [11] Squyres, S.W. et al., 1987, *Icarus, 70,* 385-408. [12] Crown, D.A. et al., 1990, this issue. [13] Watters, T.R. and D.J. Chadwick, 1989, *LPI Technical Report 89-06,* 68-69. [14] Sheridan, M.F. and K.H. Wohletz, 1983, *J. Volcanol. Geotherm. Res., 17,* 1-29. [15] Clifford, S.M. et al., 1988, *EOS (Trans. Amer. Geophys. Union), 69,* 1595-1596.

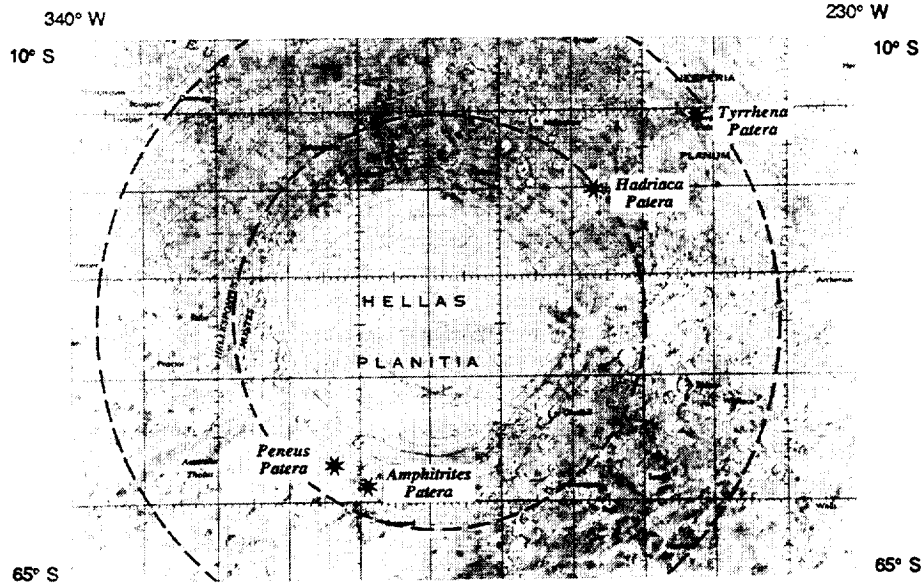

Figure 1. Portion of the *Topographic Map of Mars* showing the locations of 4 martian highland paterae. Positions of inferred basin rings (dashed lines) from Peterson, 1978.

EVOLUTION OF THE EAST RIM OF THE HELLAS BASIN, MARS

David A. Crown, Katherine H. Price*, and Ronald Greeley, *Department of Geology, Arizona State University, Tempe, Arizona 85287; *Department of Geology & Geography, DePauw University, Greencastle, Indiana 46135*

The Hellas basin, an ~2000 km impact structure with possible rings extending 4260 km in diameter [1], is a dominant feature in the ancient, southern cratered highlands of Mars. Impact basin control of volcanism and tectonism is evident on the Moon [2], and relationships between martian basins and surface processes have been identified [3-4]. The east rim of Hellas is a complex geologic region affected by volcanism, tectonism, and channeling. Remnants of an extensive mantling deposit and smooth deposits filling craters may be indicative of widespread aeolian activity, presumably related to the dust storms originating in the Hellas region [5]. A detailed study of the area between 27.5 - 42.4°S and 260 - 275°W has been initiated to analyze the processes forming surface materials and to decipher the evolution of this geologically important highland area (Figure 1). Major units include Hesperian volcanics associated with Hadriaca and Tyrrhena Paterae in the N and Hesperian and Amazonian channeled plains and outflow channels in the S. Remnants of Noachian mountains and plateaus are found throughout the region [6].

Hadriaca and Tyrrhena Paterae are low relief volcanoes thought to lie on inferred rings of Hellas [1]. The asymmetry exhibited by both volcanoes reflects the regional slope [7] caused by the topography of the basin. Materials associated with Hadriaca (Hvf) are interpreted to be ash deposits on the basis of their erosional characteristics, the low relief of the volcano, and the absence of primary lava flow features [8]. The distribution of units at both Hadriaca Patera and Tyrrhena Patera (located NE of the study area) are consistent with an origin by the emplacement of gravity-driven pyroclastic flows [8-11]. A large flank flow (Hff) containing lava flow lobes and leveed channels extends from Tyrrhena to the SW adjacent to Hadriaca Patera.

Dao and Harmakhis Valles have lengths >500 km and trend ~S45W. Outflow channel deposits have been subdivided into 3 facies: $AHch_1$, irregular materials forming channel floors, associated with channel walls, or forming dissected, low-lying regions connecting channel deposits; $AHch_2$, smooth, featureless deposits forming channel floors; and $AHch_3$, materials with linear to curvilinear features parallel to channel margins. $AHch_1$ materials are interpreted to be remnants of the plains in which the outflow channels formed and occur as sections of incompletely collapsed, dissected plains or as hummocky mounds and blocks on channel floors or slumped from channel walls. $AHch_2$ materials are smooth channel floors resulting from uniform removal of materials or uniform collapse. $AHch_3$ deposits indicate fluvial modification. These facies suggest that water flowed in part of the channels following dissection and collapse. Surrounding the channels in the S part of the mapped area is the channeled plains rim unit (AHh_5). Cross-cutting relationships N of Dao Vallis indicate that the channeling pre- and post-dates collapse.

Based upon photogeologic mapping the geologic history of the east rim of Hellas has been derived. Uplift of Noachian mountainous (Nm) and plateau (Npld, Nh_1) materials occurred in association with the Hellas impact event. The locations of mountains identify possible basin rings, which may have produced zones of weakness providing access to the surface for the magmas forming Hadriaca and Tyrrhena Paterae in Hesperian time. Erosion by runoff and/or sapping modified the plains and flanks of the volcanoes, followed by the formation of Dao and Harmakhis Valles. The presence of volatile-rich surface materials and possible fluvial or periglacial activity is suggested by the deflation and collapse of the channel deposits [12], the style of erosion of the channeled plains, and the debris aprons (AHda) and pitted materials (AHpp) observed in association with the older units. The origin and extent of the mantling deposit in the S and the role of aeolian processes are current topics of investigation. Crater counts will further constrain the temporal relationships observed.

References: [1] Peterson, J.E., 1978, *Proc. Lunar Planet. Sci. Conf., 9th,* 3411-3432. [2] Solomon, S.C. and J.W. Head, 1980, *Rev. Geophys. Space Phys., 18,* 107-141. [3] Schultz, P.H. et al., 1982, *Lunar Planet. Sci. Conf., XIII,* 700-701. [4] Schultz, P.H., 1984, *Lunar Planet. Sci. Conf., XV,* 728-729. [5] Zurek, R.W., 1982, *Icarus, 50,* 288-310. [6] Greeley, R. and J.E. Guest, 1987, *U.S. Geol. Survey Misc. Inv. Series Map I-1802B.* [7] U.S.G.S., 1987, *Topographic Map of Mars-Eastern Region, 1:15M.* [8] Crown, D.A. and R. Greeley, 1990, in *MEVTV Workshop on the Evolution of Magma Bodies on Mars,* L.P.I., in press. [9] Crown, D.A. and R. Greeley, 1988, *LPI*

Technical Report 89-04, 29-31. [10] Crown, D.A. et al., 1988, *Lunar Planet. Sci. Conf., XIX*, 229-230. [11] Greeley, R. and D.A. Crown, 1990, *J. Geophys. Res.*, in press. [12] Squyres, S.W. et al., 1987, *Icarus, 70*, 385-408.

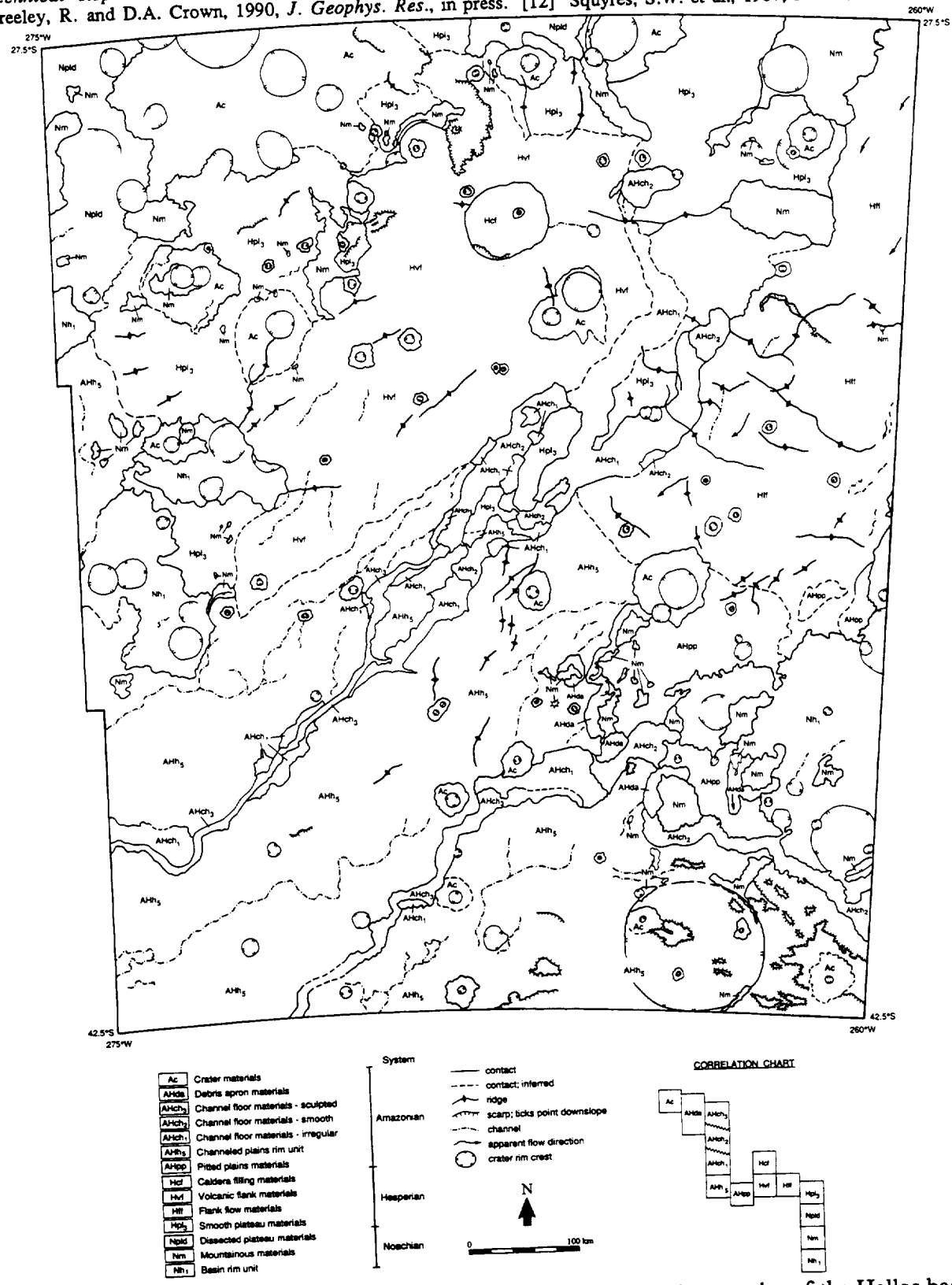

Figure 1. Geologic sketch map of the Hadriaca Patera region on the east rim of the Hellas basin.

CALCULATION OF MARTIAN GAMMA RAY SPECTRA; G. Dagge, P. Dragovitsch, D. Filges, KfA Jülich, Institut für Kernphysik,D-5170 Jülich, Germany, J. Brückner, Max-Planck-Institut für Chemie, Abteilung Kosmochemie,D-6500 Mainz, Germany

Gamma ray spectra from planetary surfaces provide a tool for the investigation of the chemical composition of the planet's surface. Galactic cosmic rays (GCR) penetrate the upper few meters of the soil producing a cascade of hadronic particles and gamma rays. Gamma rays from inelastic neutron scattering or neutron capture are a characteristical fingerprint of the target nucleus, whereas several other gamma ray sources make up a background spectrum. The gamma ray spectrum from a planetary surface thus contains information about the chemical composition of the surface material. The portion of the gamma ray flux transported back through the soil and the atmosphere can be detected from an orbiting spacecraft. Planetary gamma ray spectroscopy can be applied for a chemical mapping of planets with a sufficiently thin atmosphere like Mars, as planned for the Mars Observer Mission (launch scheduled for 1992).

In order to extract information about the Martian surface composition from measured gamma ray spectra simulations of the GCR-irradiation have to be performed. This has to be done for all subsequent processes and for a variety of material compositions and structures (1). The HERMES code system (2) allows a calculation of the complete gamma ray spectrum starting from a realistic GCR-proton (and alpha) spectrum, the supposed material composition and basic nucleon-nucleon cross sections together with cross section data for a coupled n-γ transport calculation. Therefore, modeled particle flux profiles which are often not adequate for the particular case under consideration can be circumvented. Furthermore, practically no restrictions concerning the geometry or material are imposed on the calculations.

The HERMES system is basically used for shower calculations of calorimeters and has proved its reliability for a large number of quite different applications. The analog Monte-Carlo code system consists of the four physics modules HETC/KFA-2, MORSE-CG, NDEM, and EGS-4 coupled together with a common geometry input. Particles which can not be treated by one module are stored and can be passed over to another module without loosing information about location, direction or energy. Calculations can be performed for an arbitrary 3D-geometric setup.

For a simulation of a GCR-irradiated planetary surface a proton (and alpha) source with a realistic energy distribution up to 10 GeV (40 GeV) which provides a 2π irradiation of an infinite disk is used. Since most experimental data are available from Moon, the calculational procedure was developed and tested (3,4) for this body. For the lunar case, the resulting hadronic flux profiles can be checked by calculating several production rates of nuclei such as ^{53}Mn or ^{60}Co. The agreement with experimental data is excellent (Fig. 1), which is essential for a subsequent simulation of gamma ray spectra.

For a Martian surface mapping, various gamma ray sources have to be considered. Gamma rays from (n,n'γ) and (n,γ) reactions are of main interest. For these reactions, neutrons are produced and transported by the HETC module down to energies of 15 MeV. Below that threshold, the neutrons are passed over to MORSE-CG for a coupled n-γ transport which provides the gamma ray line intensities as well as the continuum part reaching

the planet's orbit. The production of photons from inelastic neutron scattering with neutron energies above 15 MeV, spallation or from reactions such as $^{16}O(n,n'\alpha\gamma)^{12}C$ is performed by the NDEM module. This photon source is then passed over to MORSE-CG for a transport calculation. An important background source is the decay of π^0-mesons. The π^0-particles are produced by HETC and passed over for immediate decay and transport to the fourth HERMES module EGS4. A calculation for the test case Moon gives a gamma spectrum which is clearly different from earlier semi-empirical estimations concerning both intensity and spectral distribution. This background source will especially influence the investigation of low-energy gamma ray lines. Delayed photons from naturally occuring or GCR-produced radionuclides can be inserted as external source for MORSE-CG for a transport calculation.

The calculational procedure was applied for a typical Martian surface including the thin atmosphere, which proved to attenuate especially low-energy gamma ray lines (see Fig. 2). Furthermore, the HERMES system can be applied for a calculation of the gamma ray background from the GCR-irradiated orbiter at the detector site. This can be achieved by performing the same procedure as described before only by changing the geometric setup. Thus, the highly flexible code system gives access to basic problems of planetary photon production and will be an essential tool for the interpretation of measured gamma ray spectra.

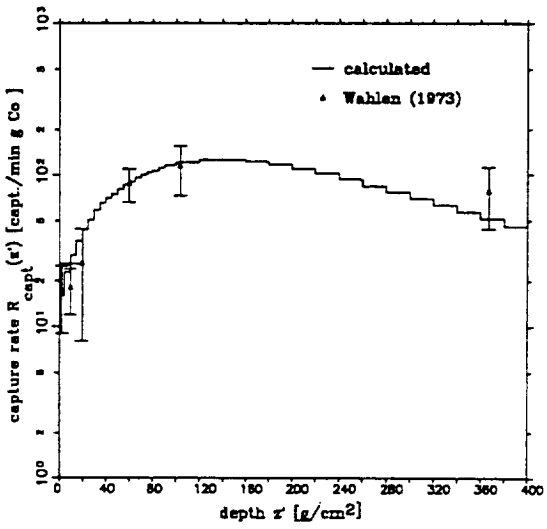

Fig. 1: Calculated depth profile of the capture rate of ^{59}Co in a lunar surface compared to experimental data from Wahlen (3).

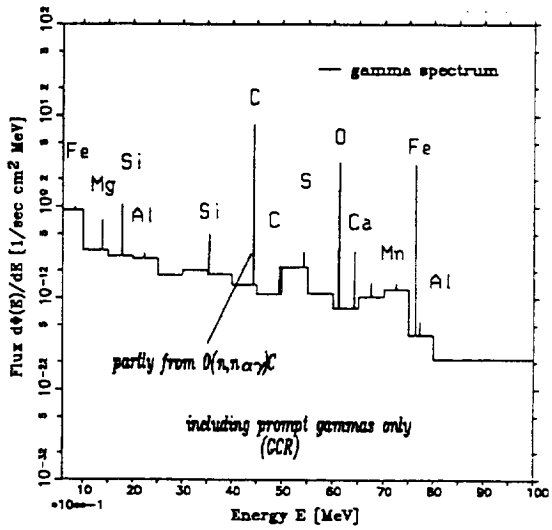

Fig. 2: Calculated spectrum of prompt photons for a typical Martian surface. Some of the most important lines were selected for the calculation.

Acknowlegdements. We wish to thank R. Michel (ZfS Universität Hannover) for providing spallation cross section data and several fruitful discussions. This work was supported by the Deutsche Forschungsgemeinschaft.

References. (1) L. G. Evans, (1987) J. Geophys. Res. Vol. 91, no. B9, p.9153-9167. (2) P. Cloth et al., (1988) HERMES User's Guide, Jül-2203. (3) M. Wahlen et al., (1973) Earth and Planet. Sci. Lett. 19, p. 315-320. (4) R. C. Reedy, (1978) Proc. Lunar and Planet. Sci. Conf. 9th, p.2961-2984.

HYDRAULIC ROUTING OF THE MAJA OUTFLOW ACROSS XANTHE TERRA:

R. A. De Hon, Department of Geosciences, Northeast Louisiana University, Monroe, LA 71209.

The object of this study is to trace a single flood crest through the Maja outflow system and to evaluate the effects of topography on ponding and multiple channel routing. Maja Valles provides a good model because it has a single source and a well-defined channel system. The 1500 km long Maja Valles originates in Juventae Chasma. The outflow system stretches 1100 km northward along the Lunae Planum--Xanthe Terra boundary, then eastward across the Xanthe Terra highlands. It descends to Chryse Planitia where it extends northeastward toward the middle of the basin.

The Lunae Planum Outflow Complex (1) includes the Maja Valles outflow and related valleys (Maja, Vedra, Maumee, and Bahram Valles) that transect Xanthe Terra and turns eastward toward Chryse Planitia. The Maja flood traveled the first two-thirds of its distance as a semi-confined sheetflood. At the northern end, it ponded on the Lunae Planum surface until the waters rose to spill over the Xanthe Terra revetment onto the lower Chryse Planitia surface. The flow first crossed the highland terrain as sheetflood flow, but broken by irregularities in the rugged highland surface, it incised a complex series of anastomosing channels (Fig.1). Early formed channels were rapidly abandoned as hanging valleys as a few main channels captured most of the drainage (2). Flow from these Xanthe canyons ponded behind the wrinkle ridge system on the western edge of Chryse Planitia (3,4). As the impounded water crested the ridges, the flood continued downslope toward the center of the basin where it lost volume by infiltration and evaporation.

During much of its brief history, the flow is marked by a single flood crest. However, multiple flood crests formed as the flow across Xanthe Terra separated into multiple anastomosing channels, then recombined in the downstream reaches. Modeling the flood surge across Xanthe Terra provides insight into the erosional and depositional history of the flood in the lower portions of the channels.

The distance across the highland is 75 km along the most direct route and ranges up to 150 km along channel routes of greatest diversion. Maumee Valles consists of 118 possible flow routes and a total of 795 km of channel segments with approximately 400 cubic km of channel storage. Vedra consists of 40 possible routes with 250 cubic km of channel storage. The "South" drainage (informal name for valley headed in the crater Dixie) consists of 6 segments and 65 cubic km of channel storage. Maja Vallis (canyon section across Xanthe) was established after the other valleys, but it eventually captured the remaining drainage from Lunae Planum.

As in any flow across a rugged surface, ponding occurred in local basins. The chief impoundments, providing more than 500 cu km of temporary storage, were in the lowland basin at 19.7°; 56.5°, the crater Bahn, the crater Dixie, the crater at 18.7°, 54.5° and the lowland trough at 17.7°; 54.3° near the mouth of Maja canyon. At these impoundments, the flood crest was delayed as the crater or basin filled to capacity. Then, one or more new flood crests formed as flood waters spilled through breaches in the downstream side of impeding basins. In the Maja canyon section, the flow onto Chryse Planitia was impeded by a highland ridge. Initially, the flow ponded in a trough on the highland side of the ridge and was diverted to the south through a 65 km relief channel. However, the flood waters eventually topped the confining ridge and cut the present gorge to allow direct drainage onto the Chryse surface.

HYDRAULIC ROUTING ACROSS XANTHE TERRA

De Hon, R. A.

Modeled times for the flow to transverse the Xanthe highland region range from 3 to 10 hours depending on flood routing and retardation within impoundments in the valley systems. Hydrographs of the flow at the termini of the chief valleys provide a graphic view of the surges as they reached the end of the valley systems. The initial flood crest was reduced to multiple surges along a prolonged flow at the terminus. Anastomosing flow was primarily responsible for reducing the initial flood crest into a prolonged flow with a series of minor ebb and flows. Ponding and release was responsible for the greatest retardations and the separation of major flood crests at the termini of the canyons.

Thus, flood routing through multiple channels and retardation in local impoundments are responsible for breakup of the initial flood crest and the formation of multiple flood crests. Recombined flow near the mouths of these canyons results in an extended flow regime and multiple flood surges. As a result of ponding along the flood course, depositional sites are localized and renewed erosion downstream (from ponded sites) results in sediment source areas not greatly removed from depositional sites. Some sites, especially at the mouths of the trans-Xanthe canyons, experienced a complex history of deposition and erosion in response to the ebb and flow of multiple flood crests imposed by flood routing and multiple ponding.

References:
1. De Hon R.A.(1987) Lunar Planet. Sci. XVIII, 227-228.
2. Greeley R. et al. (1977) J. Geophys. Res. 82, 4093-4109.
3. Thelig E. and R. Greeley (1979) J. Geophys. Res. 84, 7961-7984.
4. Baker V.R. and R.C. Kochel (1979) J. Geophys. Res. 84, 7994-8010.

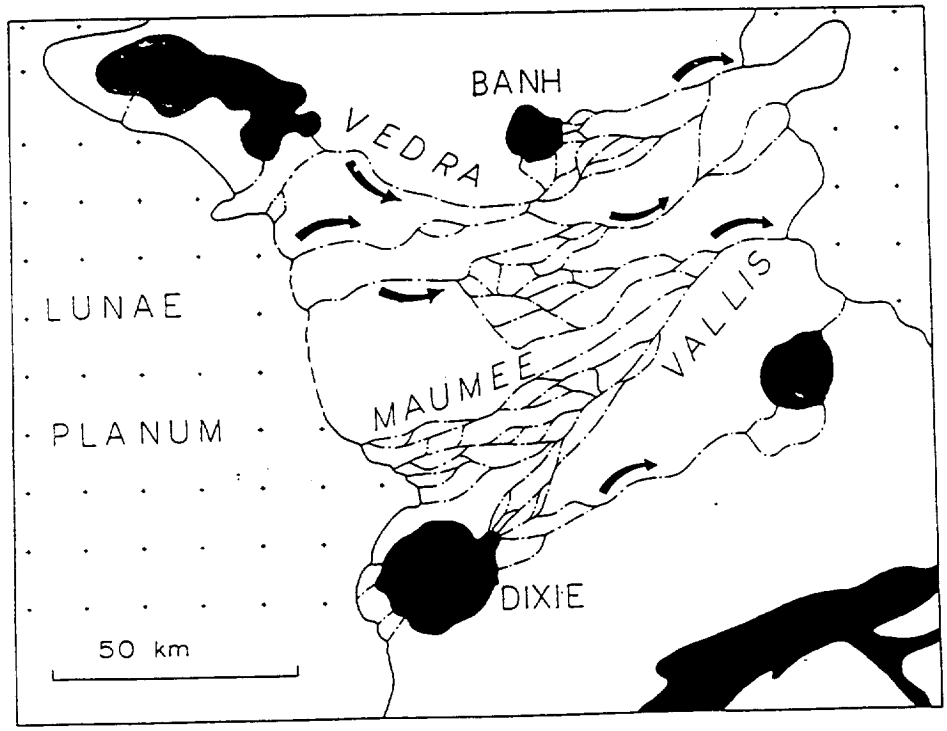

FIGURE 1. Subparallel and anastomosing channels across Xanthe Terra.

GEOLOGIC MAP OF THE GALAXIAS REGION OF MARS. R. A. De Hon, Department of Geosciences, Northeast Louisiana University, Monroe LA, 71209, P. M. Mouginis-Mark, and E. E. Brick, Planetary Geoscience Division, Hawaii Institute of Geophysics, University of Hawaii, Honolulu HA 96822.

Introduction: The Galaxias region (MTM 35217) is one of a series of 1:500,000-scale science study areas on Mars sponsored by NASA Planetary Programs. This map is part of an east-west strip which includes Hecates Tholis and a mixture of volcanic and nonvolcanic terrains near the northern limit of the Elysium lava flows. Resolution on the images used in the Viking photomosaic base ranges from 160 to 40 meter per pixel, and the solar illumination angle is not constant. Thus, visible surface detail varies considerably.

Some of the map units (Fig. 1) correspond or are partially equivalent to units of Elston (1), Scott and Carr (2), Greeley and Guest (3), and Tanaka et al. (4). Established terminology is followed where feasible, but the scale of this map requires that some new units be introduced and that some previous terminology be redefined.

Geologic Setting and Physiography: The Galaxias region is located along the transition zone between the broad Elysium Mons rise to the southeast and Utopia Planitia to the northwest. The regional topography consists of a uniform, gentle slope to the northwest upon which is superimposed a moderately smooth to rugged surface consisting of lava plains in the south and a mixture of rolling plains, rugged "badlands", and subdued knobby terrains to the north. The entrenched Hrad Vallis heads in the region and continues 500 km to the northwest. Galaxias Fossae, for which the map is named, consists of a family of parallel, deep fissures in the southern part of the region and a long, linear fissure in the northern part of the map area.

Stratigraphy: The chief stratigraphic units in the region are flows from Elysium Mons and possible volcaniclastic units associated with the Elysium activity (Fig. 1). All materials other than craters are Amazonian in age. The oldest flow material (Unit Ael1) covers much of the southern third of the map. More pristine lobate flows (Unit Ael2) are superposed on the older flows. Coarse and smooth members of the Elysium Formation (Units Aelc and Aels) form much of the surface in the northern part of the map. Smooth materials may be of clastic origin (volcaniclastic, mudflow, loess, fluvial, etc.) based on the apparent ease of dissection. The coarse member is expressed as rugged "badlands" topography that appears to form at the expense of the smooth member. Breakup of older lava flows into polygonal blocks is mapped as polygonally grooved materials (Unit Apg) along the northern edge of the flows. This material grades northward into either knobby plains material (Unit Apk) or a mixture of coarse and smooth members of the Elysium formation. Locally, lumpy plains materials (Unit Apl) consisting of closely-spaced small hillocks overlie grooved materials. Smooth plains-forming material (Unit Aps) forms broad plains and floors some basins. Fluvial materials occur as slope and floor material of the incised Hrad Vallis (Unit Ach) and as floodplain material (Unit Achp). Fluted plains material (Unit Apf) near the head of Hrad Vallis may be a lahar originating from Hrad Vallis. A unique mound of rugged ridge material (Unit Arr) stands above the plains in mid-quadrangle. Gullied or fluted slopes suggest that this material is easily eroded and may be friable volcaniclastic material or gullied domed plains material. A smaller mound is located to the southeast, and a long ridge with similar gullied or scalloped flanks is located to the east.

Craters: Most impact craters within the region are small, fresh-appearing Amazonian craters (Unit Ac). Amazonian craters have sharp rim crests and textured ejecta blankets. Some ejecta blankets extend greater than one crater diameter from the crest. Secondary crater fields are scarce. A few craters, which are partially buried by Amazonian plains-forming materials, have uncertain stratigraphic bases. These craters are designated as Amazonian and Hesperian crater material (Unit AHc).

Structure: The dominant structural trend is parallel to the regional slope. Fissures, graben, and faults trend dominantly northwest with a lesser orthogonal trend. Galaxias Fossae consists of a system of parallel and alined fissures trending northwest in the southern part of the map region and a 300 km long fissure trending west-northwest in the northern part of the region. The northwest trend is accentuated by parallel alinement of other linears such as the long axis of the rugged ridge material, other ridges, valleys, and flow lobes.

Some features present in the region are of undetermined origins. Small (1 to 3 km basal diameter) oval to elongate hillocks with apical fissures are common in the northeastern portion of the region. They may be pingos. Small ridges (less than a kilometer in width) of questionable origin occur along the edge of the smooth plains material near its contact with polygonal plains materials in the eastern portion of the area.

Channels and Hydrologic History: Hrad Vallis and an unnamed flood plain are prominent drainage courses within the map. Both drainages trend parallel to the regional slope and parallel to the dominant structural trend of fissures, faults, and lineaments. In addition, parts of Galaxias Fossae may have carried flowing water.

Hrad Vallis heads in a fissure-like depression that is locally associated with collapsed terrain. The channel is a well-defined, incised, sinuous channel flanked by a broad, paired terrace along most of its course. Slumping along the walls of the valley has left small islands of terrace material within the channel. Cut-off loops attest to an earlier period of channeling before the present channel was fully established.

East of the Hrad Vallis a flat-floored, broad, irregular depression reaches from the southeast portion of the quadrangle to beyond the central northern border. The depression has a smooth floor with some minor scour and channeling that indicates that this depression carried water. The primary source of water is a 10 km diameter depression at the northern limit of the Elysium flows, but water may have been released all along the egde of the polygonally grooved terrain. A delta and levee complex leads from the source basin into the drainage course (5). Locally, the waters embayed isolated blocks of the grooved terrain.

Geologic History: In this region, the interplay of volcanism, near surface volatiles, and surface runoff is evident. Major units were emplaced as lava flows associated with Elysium volcanism and clastic deposition as either sediment or volcaniclastic processes. Surface modification by fluvial processes and possibly by karst/thermokarst action has been responsible for the development of moderately rugged topography.

REFERENCES

(1) Elston, W. E., 1979, Geologic Map of the Cebrenia Quadrangle of Mars: U.S. Geol. Surv. Misc. Inves. Map I-1140 (MC7).

(2) Scott, D. H. and M. H. Carr, 1978, Geologic Map of Mars: U.S. Geol. Surv. Misc. Inves. Map I-1083.

(3) Greeley, R. and J. E. Guest, 1987, Geologic Map of the Eastern Equatorial Region of Mars: U.S. Geol. Surv. Misc. Inves. Map I-1802-B.

(4) Tanaka K. L., M. G. Chapman, and D. H. Scott, 1989, Geologic Map of the Elysium Region of Mars: U.S. Geol. Surv. Misc. Inves. Map I-xxxx (in press).

(5) Mouginis-Mark, P. M., 1985, Volcano/Ground Ice Interactions in Elysium Planitia, Mars: Icarus 64, 265-284.

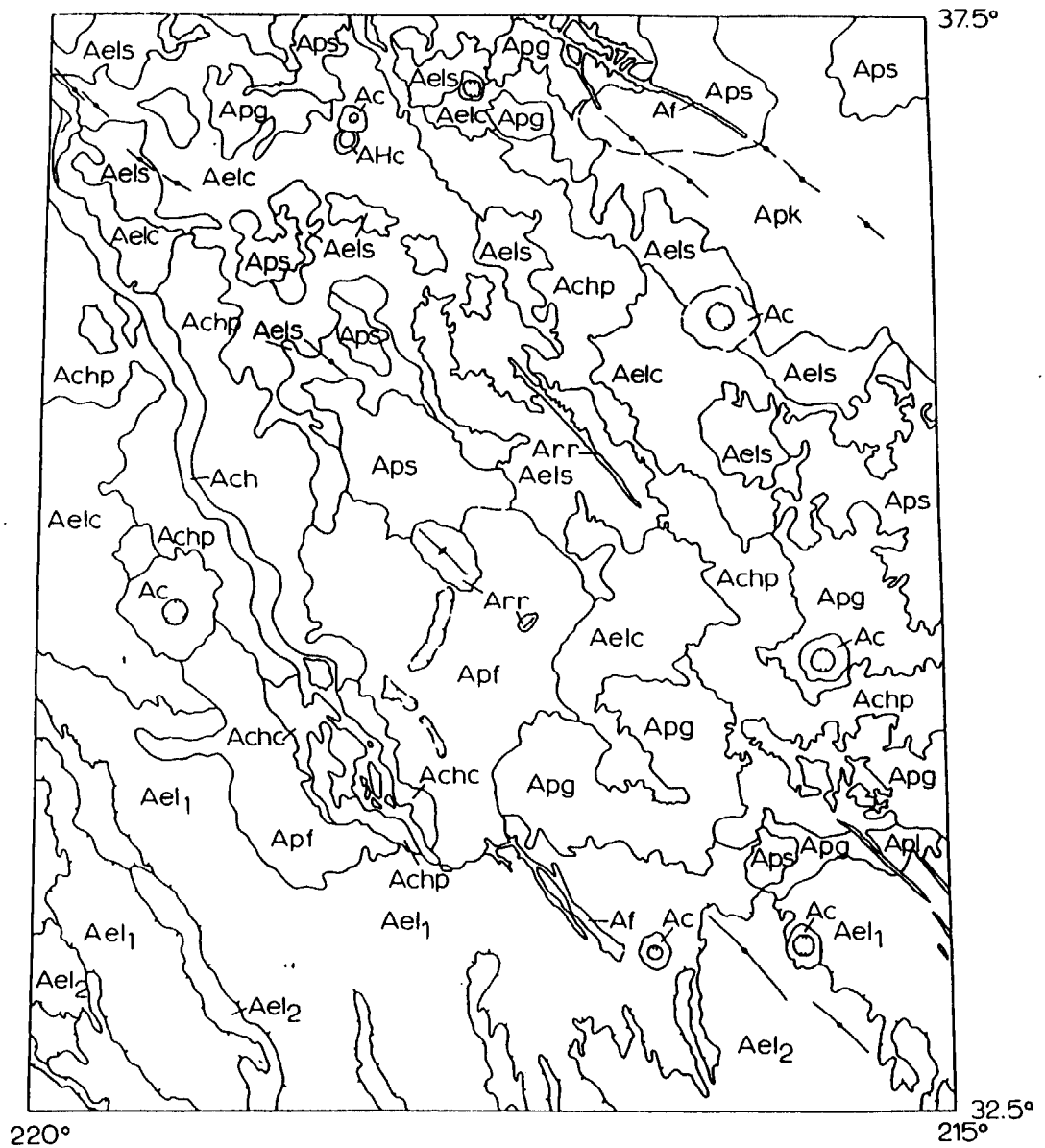

MAP UNITS

LOWLAND MATERIALS

Aps	Smooth Plains Material
Apl	Lumpy Plain Material
Apf	Futed Plains Material
Af	Fissure Material
Arr	Rugged Ridge Material
Apk	Knobby Plains Material
Apg	Grooved Plains Material

EASTERN VOLCANIC ASSEMBLEDGE

Elysium Formation

Aelc	Coarse Member
Ael_2	Member 2
Aels	Smooth Member
Ael_1	Member 1

CHANNEL MATERIALS

Ach	Channel Material
Achp	Flood Plain Material
Achc	Chaotic Channel Material

IMPACT CRATER MATERIALS

Ac	Amazonian Crater Material
AHc	Amazonian and Hesperian Crater Material

FIGURE 1. Geologic sketch map of the Galaxias Region of Mars (MTM35217).

MINIMUM ESTIMATES FOR VOLUME REMOVAL FROM THE MARTIAN FRETTED TERRAIN BETWEEN 270°W and 360°W, Andrew M. Dimitriou, University of Massachusetts, Amherst, MA 01003.

Martian fretted terrain has been a subject of study since the return of Mariner 9 data (1) and the original morphological description as offered by Sharp (1) has been widely accepted. This description is of a once continuous heavily cratered plateau which has since been subject to extensive erosion. The plateau remnants stand topographically higher as outlying "knobs" and "mesas" amidst onlapping stratigraphically younger plains materials. The best exposed area of fretted terrain on Mars lies between 270°W and 360°W in a 5-10 degree wide zone around 40°N. Work has been done in this area on the nature and origin of the debris aprons and fretted valley floor lineations (2,3) and principal component analysis attempted (4) on the outlying "mesas" in order to explain the observed distribution as a function of structural trends and erosive events. This abstract outlines the method used to estimate the volume of former plateau material that has been removed from this well exposed area of fretted terrain. The method attempts to place relatively hard lower bounds on these estimates. Upper bounds are more uncertain because inferring the extent of plateau material buried beneath plains to the north is difficult. The quantification is important because this region provides a very obvious source of material available for redistribution, and the lowlands to the north have acted as a sink for sedimentary material. The source volumes obtained here can be compared to the sink volumes required to bury large areas of the lowlands with a view to placing this regional contribution into a global context.

Three models are presented for the former extent of a once continuous heavily cratered plateau that has since been dissected and eroded. Within these model areas, outlying "mesas" and "knobs" (hereafter grouped as mountains) are separated for analytical purposes into two groups based on exposed surface area. Mountains >40 km^2 are termed large mountains, those <40 km^2 small mountains.

The southern and western limit for all three models is identical and well defined by the present boundary between fretted terrain and the heavily cratered plateau. The northern limit for all three models is less well defined because it is gradational. Between 300°W and 350°W, the northern boundary is inferred from the limit of occurrence of larger (>40km^2) mountains, which is an irregular east-west trace at about 49°N. East of 300°W, the three models have different NE limits, none of which coincides with the observed limits of fretted terrain. These northeast limits define the different model areas.

The smallest area (model 1) is bounded by a northwestward extension of the northwest trending graben sets visible on the upland surface at about 38°N, 305°W. This extension of a visible upland trend into what is now lowland is based on the postulate that the graben sets are the observable remnants of a series of northwest trending boundary faults that dissected the plateau surface and significantly dropped plateau material to the north and east. Some of the remnant mesas standing in this area of lowland appear to have long axes oriented parallel to this northwest trend. Any assumption of a continuous plateau thickness available for erosion north and east of these faults is not warranted, if this model defines the true initial northern limit of the plateau.

Model 2 includes the model 1 area but its northeast limit is farther eastward and is defined by a northwest-southeast trend at the abrupt limit of occurrence of outlying mountains. This is noted clearly around 43°N, 298°W. The rationale for this model is that this abrupt loss of mountains indicates a rapid drop in basement elevation which could be the limit of a plateau surface that has since been dissected, eroded and embayed by younger materials.

Model 3 includes all of the model 2 area and also an additional zone to the east as far as a northwest-southeast trace defined by the trend of the large irregular mesas centred on 35°N, 280°W. The mesas were identified by Wilhelms and Squyres (5) as rim remnants from their proposed 7700 km diameter Borealis basin. There is no observable evidence to indicate that a continuous thickness of plateau material was available for erosion north and east of this proposed rim boundary.

MARTIAN FRETTED TERRAIN VOLUME REMOVAL: Dimitriou, A.M.

Within all three areas, the exposed surface area of every large mountain was digitised, as was the enclosed area for each model. Shadow measurements were made at 16 locations on the continuous plateau boundary scarp and a mean height of 1.42 ± 0.52 km was determined. The quoted error not only includes the standard deviation, but a 2 pixel vertical error to account for slope rounding and shadow margin location problems as detailed by Parker et al. (6). Shadow measurements were made on 39 large mountains in a similar manner: the mean height of 1.45 ± 0.69 km agrees very well with that obtained from the scarp, strengthening the case that the mountains are remnant outliers of the plateau. In order to account for the volume of residual plateau material remaining within the model areas in the form of small mountains, five representative small subareas were located where the resolution permits a confident assessment of the surface areas and heights of small mountains to be made. An average of 3.3% of these five subareas is covered by small mountains and this is assumed to be a fair estimate across all three of the model areas. A mean height of 0.78 ± 0.41 km was obtained from 45 shadow measurements of small mountains. Ten shadow measurements were made on the margins of debris aprons visible on the extremely high resolution orbit 461B Viking images and a mean height of 0.07 ± 0.02 km was determined. Rather than attempt the extremely difficult task of identifying the percentage of the model areas covered by debris aprons, it was assumed that the entire lowland within each model area was completely buried by a debris blanket of the above thickness.

Estimates of volume removed range from 1.04 ± 0.60 M km^3 for model 1 through 1.53 ± 0.80 M km^3 for model 2 to 1.99 ± 1.10 M km^3 for model 3. This corresponds to a global equivalent sediment layer of between 3 and 21 m. If the northern lowlands is considered as the sole sink for this material a layer of between 9 and 60 m is indicated. These are minimum estimates because: (a) the thickness of plateau material measured does not represent the height above pre-plains basement but the height above the younger plains deposits (b) the northern inferred plateau limit is conservative; more plateau material may lie buried (c) the mountains were assumed to be flat-topped and have vertical cliff faces but are often conical or significantly rounded in cross-section.

As the volume of young material proposed to be present in the northern lowlands is significantly greater than that estimated above, the contribution of sediment from this area of fretted terrain is a small proportion of the lowland total.

(1) Sharp, R.P., J. Geophys. Res., 78, 4073-4083, 1973.
(2) Squyres, S.W., Icarus, 34, 600-613, 1978.
(3) Squyres, S.W., J. Geophys. Res., 84, 8087-8096, 1979.
(4) Kochel, R.C., and R.T. Peake, J. Geophys Res., 89, C336-C350, 1984.
(5) Wilhelms, D.E. and S.W. Squyres, Nature, 309, 138-140, 1984.
(6) Parker, T.J., et al. Icarus, 82, 111-145, 1989.

STRATIGRAPHY OF THE ISMENIUS LACUS SE SUBQUADRANGLE: CLUES TO AN UPLAND/LOWLAND BOUNDARY FORMING EVENT?, Andrew M. Dimitriou, University of Massachusetts, Amherst, MA 01003.

The Ismenius Lacus SE (MC5SE) subquadrangle is located in NE Mars between 292.5^{0}W and 315^{0}W and 30^{0}N and 47.5^{0}N. Within this area, the global boundary between southern heavily cratered upland and northern sparsely cratered lowland is well exposed along a series of northwest trending scarps that approximate 1.4 km in mean height (1). To the northwest and southeast of the boundary defined by the scarps, areas of "fretted terrain" (2) make the upland/lowland boundary difficult to locate precisely. Geologic mapping based on Mariner 9 imagery was done by Lucchitta (3) over the entire MC5 quadrangle at a scale of 1:5M. This area was also covered in the 1:15M scale map of the Martian eastern hemisphere as compiled by Greeley and Guest (4). The purpose of this abstract is to present the initial results of a stratigraphic and tectonic study of this area using the highest available resolution Viking imagery as well as the published 1:2M photomosaic. By obtaining a detailed relative age sequence of the geologic units isolated, the fracturing and tectonic history of this key upland/lowland boundary area can be constrained more precisely than before. The cumulative crater plots generated were compared with the Neukum and Hiller curve (5) and stratigraphic ages assigned with reference to Tanaka (6).

Within the uplands, a distinctive population of "rimless" craters is recognised which has also been noted in Amenthes (7). It is assumed here that these craters represent an old population lying at a relatively uniform depth beneath the present plateau surface units. When relative ages are determined, either by considering the plateau surface as a whole or by separating populations based on the observable geologic units, counts of "rimless" craters yield an Early Noachian age.

Above this ancient surface, a number of geologic units can be identified based on differences in surface morphology. A smooth plateau unit is located along the fretted northern boundary of the plateau and as a capping unit on the outlying mesas. This is interpreted as being volcanic and/or aeolian material and yields a crater age of Early Amazonian. The smooth plateau unit truncates a boundary between two units tentatively interpreted as volcanic, the most extensive of which is identified as ridged plateau. It lies in the central portion of the upland in this subquad and is characterised by the presence of low relief irregular scarps; crater counts yield a Early Hesperian age although the counts also indicate that lava may have continued to flood this surface with decreasing volumes into the Early Amazonian. The ridged plateau is fractured and truncated along its eastern margin by boundary scarps which separate upland from lowland materials. The second unit truncated by the smooth plateau is characterised by a hummocky surface at km scale and is thus identified as hummocky plateau. This is located in the central and eastern portion of the upland where its eastern margin is also dissected and truncated by boundary scarps. Crater counts yield an Late Hesperian age for this unit.

A complexly eroded unit is identified in the southern region of the subquad as etched plateau. The boundary between this and the ridged plateau is characterised by erosional rather than depositional processes. Here, the visible etched unit consists of ridged and possibly smooth plateau material that has been differentially eroded in a complex manner leaving irregular and circular positive relief landforms. Crater ages from this unit yield Early Amazonian ages, but this relative youth is almost certainly due to removal of craters by the complementary processes of erosion and deposition, the stratigraphic age of the materials visible is older. These erosional and depositional processes have neverless allowed a fairly clear boundary to be drawn between the etched and ridged units.

Within the lowland along the upland/lowland boundary, a unit which is characterised by the presence of bright, very sparsely cratered material is identified. This unit includes debris aprons present at the base of the scarp and of many outlying mountains and also bright deposits mantling the floors of fractures and irregular valleys penetrating into the uplands. Crater counts proved impossible on this unit due to the small number of superposed craters present.

North and west of the boundary scarp, three lowland plains units are identified: a smooth plains unit, a very smooth plains unit and an etched plains unit. Crater counts are only possible

on the first two units and yield ages between Early and Middle Amazonian. The latter unit does not have a large enough exposed area within the mapped area to permit crater counting. The morphological differences between the first two units is based on the relative abundance of small mountains that are scattered through the lowland plains. These mountains are inferred to represent inliers of older material. Within the areas where these mountains abruptly decrease in abundance practically to zero the very smooth plains unit was identified. The differences in mountain abundance are taken to represent variations in sub-plains basement elevation. The etched plains unit is characterised by the presence of small (< 10km long axis) cuspate positive relief features that suggest differential erosion of plains materials.

A unit that consists of isolated large groups of mostly rounded mountains scattered in a wide zone roughly paralleling the present trace of the upland/lowland scarp is interpreted to be remnants of an older surface that has been partially buried and embayed by the unconformable younger plains materials. Crater remnants are visible in many cases and counts over these areas yield a population that fits the Neukum and Hiller production curve (5) very well. The age determined is Early Noachian. Therefore, the surface that lies at a shallow depth on the plateau is also present at a shallow depth in the lowlands, an elevation difference of at least 1.4 km.

In order to account for this observation, work is in progress attempting to model this as an area which experienced crustal downwarping, or normal faulting causing downthrow to the northeast. These models must also take into consideration the timing of the event. Because some of fractures cut upland surfaces the faults are inferred to have initiated around the Late Noachian/Early Hesperian boundary, which is significant for the timing of the origin of the dichotomy boundary itself in this region of Mars.

This region is a key area of the upland/lowland boundary, due to the exposure of a wide age range of materials. The work done and the modelling in progress enables better constraints to be placed on the timing and nature of this portion of the global dichotomy.

(1) Dimitriou, A.M., Lunar and Planet Sci. Conf. XXI (abs), this volume, 1990.
(2) Sharp, R.P., J. Geophys. Res., 78, 4073-4083, 1973.
(3) Lucchitta, B.K., Geol. Map Ismenius Lacus Quadrangle of Mars, Map I-1065, 1978.
(4) Greeley, R. and J.E. Guest, Geol. Map of Eastern Equatorial Regions of Mars, Map I-1802B, 1987.
(5) Neukum, G., and K. Hiller, J. Geophys. Res., 86, 3097-3121, 1981.
(6) Tanaka, K.L., J. Geophys. Res., 91, E139-E158, 1986.
(7) Maxwell, T.A. and R.A. Craddock, Lunar and Planet Sci. Conf XX (abs),646-647, 1989.

EXPERIMENTAL SIMULATION OF MARTIAN NEUTRON LEAKAGE SPECTRUM; D.M. Drake, S. Wender, R. Nelson, and E. R. Shunk, Los Alamos National Laboratory, Los Alamos, NM 87545; Winfried Amian, UFA, Julich, FRG; Peter Englert, San Jose State University, San Jose, CA; Johannes Bruckner, Max-Planck Institut fur Chemie, Mainz, FRG; Manfred Drosg, University of Vienna, Vienna, Austria

The boron loaded plastic scintillator that partially surrounds the Gamma Ray Spectrometer (GRS) of the Mars Observer satellite has two functions. First, via anticoincidence, it allows pulses that are caused by energetic cosmic rays to be eliminated from the gamma-ray spectrum, and second, it counts cosmic ray created neutrons that leak from the martian surface. Due to the fact that the plastic shield is divided into four parts similar to the sides of a pyramid, the neutron leakage spectrum can be parameterized by the four counting rates. Because the space craft velocity is larger than that of thermal neutrons, the front face of the counter counts faster than the back face.[1]

In a previous paper[2], we modeled the neutron leakage spectrum using a neutron transport code for various martian surface conditions (dry and wet regolith, layers, and carbon dioxide overlay). These spectra were parameterized into epithermal and thermal parts in order to facilitate identification regolith features.

Although we have a high degree of confidence in the codes used, we thought some experimental verification of the trends predicted would be appropriate.

To this end we filled a large container with pseudo "martian sand" whose composition was similar to that found at Chryse and bombarded it with pseudo cosmic rays, i.e., 800 MeV protons from the Los Alamos LAMPF accelerator.

The LAMPF beam was delivered in pulses whose time duration was less than a nano-second, about twenty time per second. The leakage neutrons were detected by ^{6}Li glass detectors located at the end of a 30 meter evacuated flight path. The time of flight neutron spectra were converted to energy spectra and corrected for detector efficiency so that they could be compared directly to the calculated spectra.

Preliminary results of this experiment show the neutron spectrum to be considerably harder than calculations using infinite plane geometry. We attribute this difference in part to the finite size of the containers.

References

1) William C. Feldman and Darrell M. Drake, Nuclear Instruments and Methods A245 (1986) 182.

2) D. M. Drake, W. C. Feldman, and B. M. Jakosky, Journal of Geophysical Res. 93 (1988) 6353.

A GAMMA RAY MODE OF THE ALPHA PARTICLE ANALYTICAL INSTRUMENT

Thanasis Economou* and Anthony Turkevich *#.
* Laboratory for Astrophysics and Space Research, Enrico Fermi Institute,University of Chicago, Chicago, # Chemistry Department, University of Chicago, Chicago, IL 60637.

The Alpha Particle Analytical Instrument provided the first relatively complete analyses of lunar surface material at three locations on the moon during the Surveyor Missions in 1967 and 1968 using only the classical alpha and proton modes of the technique. The capabilities have since been expanded by measuring the fluorescent x-rays produced by the interaction of the source radiations with the sample surface. Such versions of the instrument were flown on the ill-fated Soviet Phobos missions in 1988. The alpha sources used in such instruments are also neutron emitters due to spontaneous fission branches in the alpha decay and due to the interaction of the alpha particles with nearby materials. These neutrons can react with surrounding materials to produce gamma rays. Inclusion of a gamma ray detector in the Alpha Particle instrument can enhance the analytical capabilities of the package by providing a direct sensitivity for hydrogen, by providing a bulk analysis for several elements that are determined in the surface material, and by providing some isotopic information. This possibilitiy of determining several elements by different modes can remove ambiguities about the applicability of a surface analysis to represent bulk composition. Thus, an alpha particle package with alpha, proton, x-ray and gamma modes can provide the most complete in situ chemical analysis of an extraterrestrial body that is presently possible.

In order to test these ideas a 50 mCi ^{244}Cm alpha source, mounted on stainless steel, has been used in an arrangement where the alpha (neutron) source was approximately 20 cm away from a cooled 30 cm^3 GeLi crystal. Samples of various materials, varying in mass from 2 to 15 Kg were interposed between the source and detector and the resultant gamma rays measured. The experimental situation differs from that of Bruckner et al (1) in using relatively low energy neutrons (less than 4 MeV cf 14 MeV) and rather thick targets.

As an example of the type of results obtained, Figure 1 compares the response of the gamma detector to a sample of $NaHCO_3$ with that when Na_2CO_3 is the sample. Figure 1a shows the energy region between 420 and 500 KeV. Also shown is the detector response when no sample is present. Clearly seen in both carbonate samples is the 439 KeV gamma ray line due to inelastic neutron scattering on ^{23}Na. In the NaHCO3 sample there is, barely visible, the 472 keV neutron capture line in ^{23}Na. This line is not seen in the Na_2CO_3 sample presumably because of neutron leakage before capture.

Figure 1b shows the spectra in the 2 MeV region. The 2.22 MeV neutron capture line of hydrogen is visible in the bicarbonate sample. The neutron capture lines of H and ^{23}Na are greatly enhanced by addition of surrounding paraffin.

Table I lists the samples that have been measured so far, the gamma rays identified and their relative intensities as recorded. These preliminary results should be used with caution since the intensities will depend on the actual geometrical situation which, in this work, was quite different from that to be encountered on either a surface or penetrator type space mission.

The gamma rays detected so far are pretty much those expected by calculations of the type of Evans et al (2) although some significant differences are noted. For example, in the magnesium run, the lines at 1.369, 1.612 and 1.809 MeV are not in the ratios given by Evans et al (2), and the 1.612 MeV line is hardly visible in our measurements. In addition, the detector system used here had a cut off at 6.1 MeV and was too small to have a good efficiency for gamma rays above about 4 MeV.

On a space mission with alpha sources of the strength needed for the alpha and proton modes of the Alpha Particle Instrument, the gamma ray rates should be at least comparable to those expected from cosmic rays. They could easily be enhanced by up to a factor of ten by use of a Be shutter over the alpha sources or with higher intensity, encapsulated, alpha sources.

There are several disadvantages to using such neutron sources for exciting gamma rays for analytical purposes and these have to be investigated. However, advantages would be the presence of a neutron source of constant and known strength and energy distribution, the response to which could be adequately calibrated on earth. This would make the analytical results quantifiable in a way hard to do with cosmic ray activation.

Acknowledgements: Support provided by the U.S. National Aeronautics and Space Agency (grant #NAG W 878).

References: (1) J. Bruckner, R.C. Reedy and H. Wanke, Lunar and Planetary Sci. XV, Abstract p. 98 (1984). (2) L.G. Evans, J.I. Trombka and W.V. Boynton, Lunar and Planetary Sci. XVI, J. Geophys. Res. 91, D525 (1986).

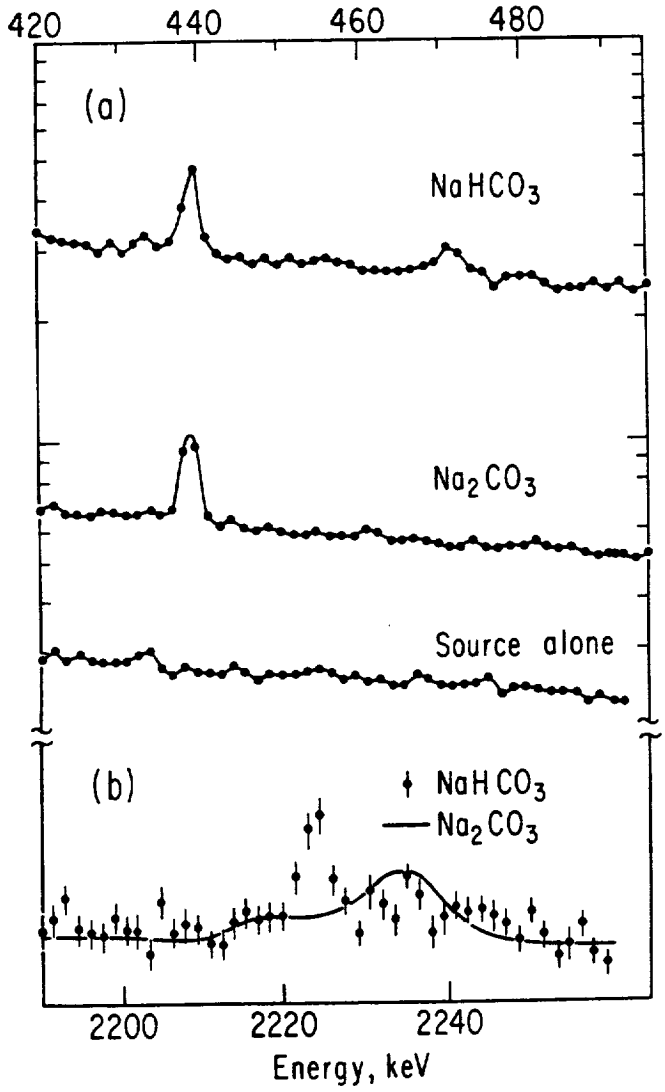

Fig.1 Response of Ge(Li) detector to carbonate samples exposed to 50 mCi ^{244}Cm. 1a: Energy region 420-500 keV. 1b: Energy region 2150 -2260 keV

TABLE I

Sample	Weight (kg)	Line	Isotope	Relative Intensity (c/1000 min)
Plexiglas	5.9	2,223	H	3936 ± 70
Na_2CO3	12.0	439	^{23}Na	5088 ± 146
NaHCO3	10.0	439	^{23}Na	802 ± 52
		472	^{23}Na	263 ± 47
		2,223	H	70 ± 13
Mg	5.4	1,369	^{24}Mg	1355 ± 74
		1,612	^{25}Mg	236 ± 22
		1,819	^{26}Mg	263 ± 47
Al	15.0	2,210	^{27}Al	167 ± 16
SiC	2.8	1,779	^{28}Si	288 ± 28
		1,273	^{29}Si	717 ± 47
		2,235	^{30}Si	746 ± 31

THE X-RAY MODE OF THE ALPHA PARTICLE ANALYTICAL INSTRUMENT

T. Economou*, J. Iwanczyk** and A. Turkevich*

*Laboratory for Astrophysics and Space Research, The University of Chicago,Chicago, Il.60637.
**Xsirius Scientific,Inc. 4640 Admiralty Way, Suite 214, Marina Del Ray, California 90292.

The Alpha Particle Instrument with its alpha, proton, x-ray, and now, the new gamma ray modes, is a versatile analytical instrument that can provide the most complete in-situ chemical analyses of samples on planetary missions. The instrument is based on interactions of radiation with matter that are well understood and it can be easily calibrated in the laboratory before being sent into space. Its performance has been proven during space missions in the past.

The excitation of characteristic x-rays in the Alpha Particle instrument is caused by two mechanisms: 1) by the alpha particles from the curium radioactive source - the same source that is used in the alpha, proton and the gamma modes - and, 2) by the plutonium L x-ray lines (14-22 keV) which are more effective than alpha particles in exciting higher Z elements. Such excitation is sufficient to obtain good analyses for all the major elements in relatively short counting periods. To enhance the sensitivity for certain minor and trace elements, additional auxiliary x-ray excitation sources can be utilized (e.g ^{109}Cd , ^{241}Am, etc).

In the past, (e.g. on the recent Soviet Phobos mission), the X-ray mode of this instrument was implemented by using a cryogenically cooled Si(Li) detector. However, for many missions, including a mission to Mars, such cooling is impractical or impossible. In such cases ambient temperature x-ray detectors are needed. (J. Iwanczyk et al, 1986, 1989).

We report here the first preliminary results obtained using an x-ray probe containing an ambient temperature HgI_2 x-ray detector attached to the Alpha Particle instrument as shown in Fig. 1. The detector used in this work had an area of 5 mm^2 with about 500 mm depletion depth . It was biased at -800V. The detector and the first stage FET transistor were slightly cooled to about 0° C by small Peltier coolers. Such cooling will not be necessary for most missions . The detector was exposed to the x-rays from the sample in vacuum and acted therefore as a windowless detector. A 3.5 mm parylene N type film was coated directly on to the HgI_2 crystal to prevent contamination and to enable the detector to operate properly in vacuum. The total energy resolution of the x-ray system was 225 eV at 6.04 keV of Fe K_a line The electronic noise was 187 eV.

With this arrangement we were able to detect the very low x-ray energies that even the best laboratory silicon detector with thin Be window have difficulties detecting. Fig. 2 shows the x-ray spectrum obtained from a Na_2CO_3 sample. The sodium line at 1.04 keV is clearly above the noise level of the system. Fig.3 shows the x-ray spectrum obtained from a sample of an Allende meteorite There, the 1.25 keV Mg K_a line is well separated from 1.74 keV Si K_a line. With proper line fitting algorithms even a line from about 1.7 % aluminum (1.49 keV) sample can be detected in the presence of 15% Mg and 13% Si present in the Allende meteorite . The other lines are due to sulphur, calcium, titanium,chromium,manganese,iron and nickel. Notice that the Fe K_b line is very well separated from the Ni Ka line. Fig.4 shows for comparison a similar spectrum obtained with the Phobos x-ray instrument that utilized cooled Si(Li) detectors (Hovestadt et.al.,1988.).

Although the first results of the x-ray mode of the Alpha Particle instrument using ambient temperature HgI_2 x-ray detectors were much better than we had expected in terms of

resolution and sensitivity to low energies, it can be seen that the Phobos instrument with similar energy resolution has slightly better sensitivity to elements present in low concentration This is due to the higher background in the present arrangement. As can be seen from Fig.1, the source-sample-detector geometry of the x -ray probe is less than optimal in this experimental setup. By mounting the x-ray detector inside the Alpha instrument, the sample to detector distance can be decreased from the present 65 mm to less than 25 mm. This will increase the useful x-ray counting rate by almost a factor of seven while the background will not change significantly. This will dramatically improve the sensitivity of the instrument to low concentration elements. Future experiments will concentrate on investigating the best design geometries, detector sizes and the best auxiliary excitation sources.

Acknowledgements. The present work was supported by the U.S. National Aeronautics and Space Agency (grant # NAGW-1847 and # NASW-4492)

References: J. S. Iwanczyk, A. J. Dabrowski, G. C. Huth, J.G. Bradley, J.M Conley and A. L. Albee, Low Energy Spectra Measured with Mercutic Iodide Energy Dispersive Spectrometer in Scanning Electron Microscope, IEEE Tran. Nucl. Sci. Vol. No.1, 355-358 (1986).

J.C Iwanczyk, Y.J.Wang,J.G.Bradley,J.M.Conley, A.L.Albee, and T. E. Economou , Performance and Durability of HgI_2 X-ray HgI_2 Detectors for Space Missions IEEE Tran Nuc Sci, Vol.37, No.1 pp.841-845 (1989).

D. Hovestadt. et all : In-situ Measurements of the Surface Composition on the Phobos Mission. Lunar and Planetary Science XIX (March 14-19,1988), p.511.

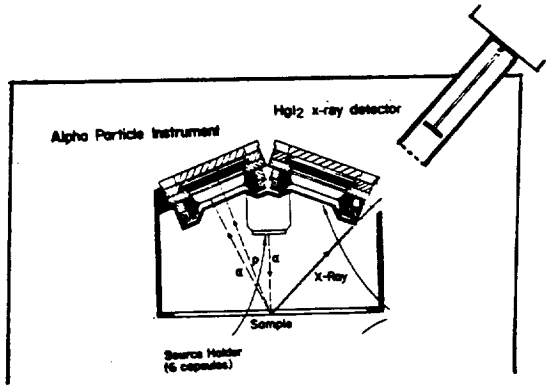

Fig. 1: Geometrical relationship of HgI_2 detector probe attached to the Alpha Particle Instrument.

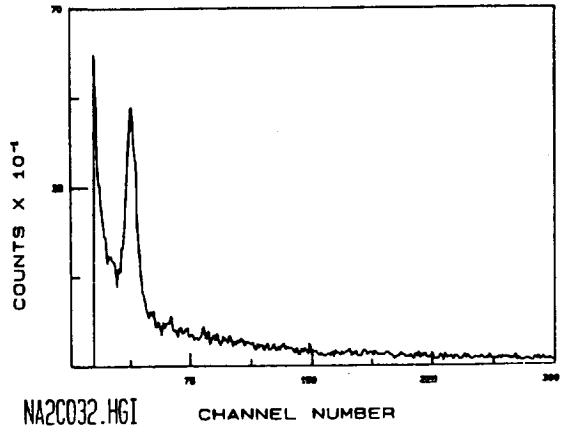

Fig. 2: Sodium K_a line at 1.04 keV from Na_2CO_3 sample. The resolution of the line is 180 eV.

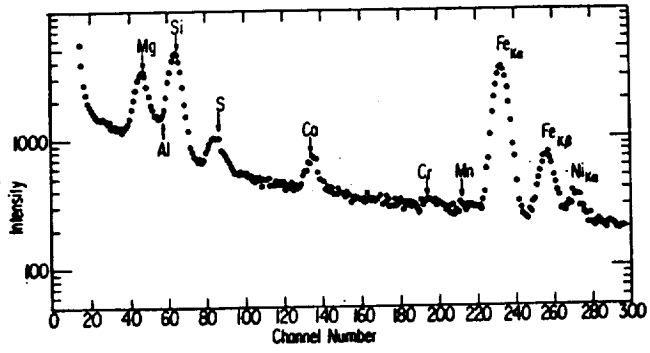

Fig. 3: X-ray spectrum from a sample of meteorite Allende, obtained with HgI_2 x-ray detectors at ambient temperature . The sample was excited with 40 mCi of ^{244}Cm alpha source that is used by the Alpha Particle instrument.

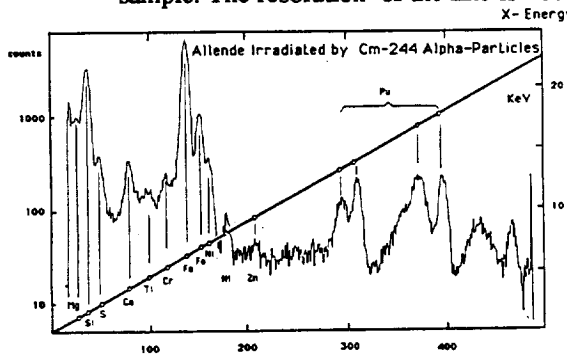

Fig. 4: X- ray spectrum from similar Allende sample obtained with Phobos Alpha-X flight instrument that utilized cooled Si(Li) detector and ^{244}Cm source excitation.

POSSIBLE CINDER CONES NEAR THE SUMMIT OF PAVONIS MONS, MARS.

Kenneth S. Edgett, Department of Geology, Arizona State University, Tempe, AZ 85287.

Introduction. In 1979, Wood [1] mentioned the existence of a possible cinder cone near the summit of Pavonis Mons, and he estimated its dimensions. Examination of medium resolution *Viking* photographs has revealed four additional candidate cinder cones in the summit region. Pavonis Mons has been largely overlooked in the literature concerning the late-stage volcanic activity of the Tharsis volcanoes; and no cones have been found on the other Tharsis Montes [2,3]. The presence of possible cinder cones near the summit implies that volatile-rich pyroclastic activity occured late in the evolution of Pavonis Mons.

Setting. The summit region of Pavonis Mons (Fig. 1) was photographed at moderate to high resolution (50 to 75 m/pixel) by both *Mariner 9* and *Viking 1*. The summit is about 18 km above the martian datum [4,5], and has two conspicuous features: a 45 km-diameter caldera and, off-set to the northeast, an 85 km-diameter depression [6-9]. The caldera is about 4 to 5 km deep [4,5,10]; and the walls have numerous vertical, parallel ridges and grooves which are attributed to mass wasting and aeolian modification [11,12]. The caldera floor appears smooth and featureless with the exception of two 500 m-diameter craters. The large depression is bounded by inward-facing arcuate scarps in the west, and both an inward- and outward-facing scarp in the east. There is no surface expression of the southeastern rim of the depression. Six mare-type wrinkle ridges oriented radial to the caldera occur within the depression, none occur within 5 km of the caldera rim, but three of them extend up to 12 km beyond the depression rim. The depression apparently formed before the caldera; and the wrinkle ridges formed before or concurrently with the depression [13]. The wrinkle ridges likely formed by compression [14-16], the depression likely formed by volcano-tectonic collapse [9].

Cones and Mounds. Five cones or mounds, labeled "c" in Fig. 1, occur within 5 km of the caldera rim. The best example is a cone with a pit at its summit which occurs on the volcanic shield along the edge of a fissure, about 3.5 km west of the caldera rim. This cone, originally identified by Wood [1], is best seen in an oblique-view photograph from *Mariner 9* (DAS 55663953). It is also visible in *Viking 1* images 210A32 and 210A34. To the north of this cone there is an irregular, rough-textured, raised-relief landform (labeled "m" in Fig. 1) which is bissected by a fissure. Two mounds, approximately elliptical in shape, occur along fissures north of the caldera rim between the rim and the southern end of a wrinkle ridge in the 85 km depression; one of these features appears to have a summit crater. Two additional features, circular mounds with summit pits, are visible near the limits of resolution in *Viking* frame 210A34; they occur in the large depression about 15 km east of the elliptical mounds and about 5 km north of the caldera rim.

Interpretations and Discussion. The five cones and the irregular, rough-textured landform are considered to be volcanic constructs, because of their occurence on a volcano and their proximity to both the caldera and to fissures in the summit region. Wood [1] interpreted the cone seen in the *Mariner 9* image as a possible cinder cone with a basal diameter of ~1.1 km, a crater diameter ~0.45 km, and a height of ~0.07 km. Although Wood did not plot this cone [fig. 6 of 1], with these dimensions the cone plots within the cinder cone "field" of Wood's crater diameter/basal diameter diagram for monogenetic volcanoes [13].

Alternative explanations for the cones are: (1) They could be small effusive volcanoes, such as the chain of low shields in the Arsia Mons caldera [17]; or (2) they could be volcanic domes. Short of obtaining very high resolution photographs or thermal infrared measurements, there is no conclusive test to demonstrate that any of the five cones/mounds are cinder cones. One test for the presence of cinders is to look for very high resolution thermal infrared data, which might indicate the presence of cinders because thermal inertia correlates with grain size under martian atmospheric conditions [*eg.* 18]. The highest resolution thermal infrared data from the *Viking* Infrared Thermal Mapper (IRTM) did not indicate the presence of surficial deposits with grain sizes larger than ~0.1 mm (silt-sized) on the Pavonis Mons shield [19]. However, the spot sizes for these data were about 3 to 5 km, while the cones are smaller, about 1 to 3 km.

If the cones are cinder cones, then they indicate that pyroclastic activity occured on Pavonis Mons. Since they appear to be associated with fissures emanating from the caldera, they might post-date the caldera collapse, and would therefore suggest that the last summit volcanic activity involved volatile-rich magmas [*eg.* 20]. Cinder cones form from short-lived strombolian eruptions, usually resulting from eruption of a low-viscosity magma through a narrow fissure or conduit [21]. The fact that these landforms do not resemble the low-profile, several km-wide cinder cone shapes predicted for Mars by McGetchin *et al.* [22] might be explained by their use of terrestrial values for ejecta volumes, escape angles, and velocities.

The possible presence of cinder cones on Pavonis Mons distinguishes it from the other Tharsis volcanoes. Olympus, Arsia, and Ascraeus Montes were photographed at higher resolutions by the *Viking Orbiters*, yet detailed studies of these volcanoes reveal no cinder cones or other evidence for pyroclastic volcanism [2,3]. It should be noted that the Hawaiian basaltic shield volcanoes have numerous cinder cones on them [*eg.* 23]; suggesting that Pavonis Mons has had a similar evolution.

The cone-shaped landforms near the summit of Pavonis Mons are the most likely candidate cinder cones yet identified on Mars, because they occur on a volcano and they occur in the vicinity of a caldera, as do many of the Hawaiian cinder cones. Possible cinder cones have also been identified on Elysium Mons

CINDER CONES ON PAVONIS MONS? *K.S. Edgett*

[24]. Numerous cone-shaped features with summit pits have been identified elsewhere on Mars [*eg.* 25-27], but their volcanic associations are questionable due to the lack of a definite volcanic context.

References: [1] Wood, C.A. (1979) *Proc. 10th Lunar Planet. Sci. Conf.*, 2815-2840. [2] Mouginis-Mark, P.J. (1981) *Proc. 12th Lunar Planet. Sci. Conf.*, 1431-1447. [3] Zimbelman, J.R. (1984) PhD Diss., Arizona State Univ.; reprinted in (1986) *Adv. Planet. Geol., NASA TM 88784*, 271-572. [4] Hord, C.W. *et al.* (1974) *Icarus, 21*, 292-302. [5] U.S. Geol. Surv. (1989) Topographic Maps...of Mars; *Map I-2030*, 1:15M scale. [6] Masursky, H. *et al.* (1972) *Science, 175*, 294-305. [7] McCauley, J.F. *et al.* (1972) *Icarus, 17*, 289-327. [8] Carr, M.H. (1973) *J. Geophys. Res., 78*, 4049-4062. [9] Crumpler, L.S. and J.C. Aubele (1978) *Icarus, 34*, 496-511. [10] Bibring, J.-P. *et al.* (1989) *Nature, 341*, 591-593. [11] Sharp, R.P. (1973) In *Geology, Seismiscity, and Environmental Impact* (D.E. Moran *et al.*, eds.), pp. 115-122, Assoc. Eng. Geol., Univ. Publ., Los Angeles. [12] McCauley, J.F. (1973) *J. Geophys. Res., 78*, 4123-4137. [13] Edgett, K.S. and J.R. Zimbelman (1990) "The Landforms of Pavonis Mons, Mars," (manuscript in preparation). [14] Baldwin, R.P. (1963) *The Measure of the Moon*, Univ. Chicago Press, 488p. (see p. 380). [15] Plescia, J.B. and M.P. Golombek (1986) *Geol. Soc. Am. Bull., 97*, 1289-1299. [16] Watters, T.R. (1988) *J. Geophys. Res., 93*, 10236-10254. [17] Carr, M.H. *et al.* (1977) *J. Geophys. Res., 82*, 3985-4015. [18] Kieffer, H.H. *et al.* (1973) *J. Geophys. Res., 78*, 4291-4312. [19] Zimbelman, J.R. (1986) *Trans. Am. Geophys. U. (EOS), 67*, 1074. [20] Blackburn, E.A. *et al.* (1976) *J. R. Soc. London, 132*, 429-440. [21] Wilson, L. and J.W. Head (1981) *J. Geophys. Res., 86*, 2971-3001. [22] McGetchin, T.R. *et al.* (1974) *J. Geophys. Res., 79*, 3257-3272. [23] MacDonald, G.A. *et al.* (1983) *Volcanoes In The Sea; The Geology of Hawaii*, 2nd ed., Univ. Hawaii Press, Honolulu, 517p. [24] McBride, K. and J.R. Zimbelman (1989) *Lunar Planet. Sci. XX*, 651. [25] Woronow, A. (1980) *Repts. Planet. Geol. Prog.-1979/80, NASA TM 81776*, 187-188. [26] Plescia, J.B. (1980) *Repts. Planet. Geol. Prog.-1980, NASA TM 82835*, 263-265. [27] Frey, H. and M. Jarosewich (1982) *J. Geophys. Res., 87*, 9867-9879. [28] **Acknowledgements:** Comments by J.R. Zimbelman and D.A. Crown were very helpful in refining the discussion presented here.

Figure 1. Sketch map of the summit region of Pavonis Mons. Mare-type ridges are shaded. The five cone-shaped features are labeled "c", and are interpreted as *possible* cinder cones. Feature (m) is interpreted to be a volcanic extrusion which post-dates the caldera. The units labled are: (cf)= caldera floor, (s)= wall-slump material, (cw)= caldera walls. Sketch is centered at 0.8°N, 112.7°W; the map base included *Viking 1* images 210A 33-36.

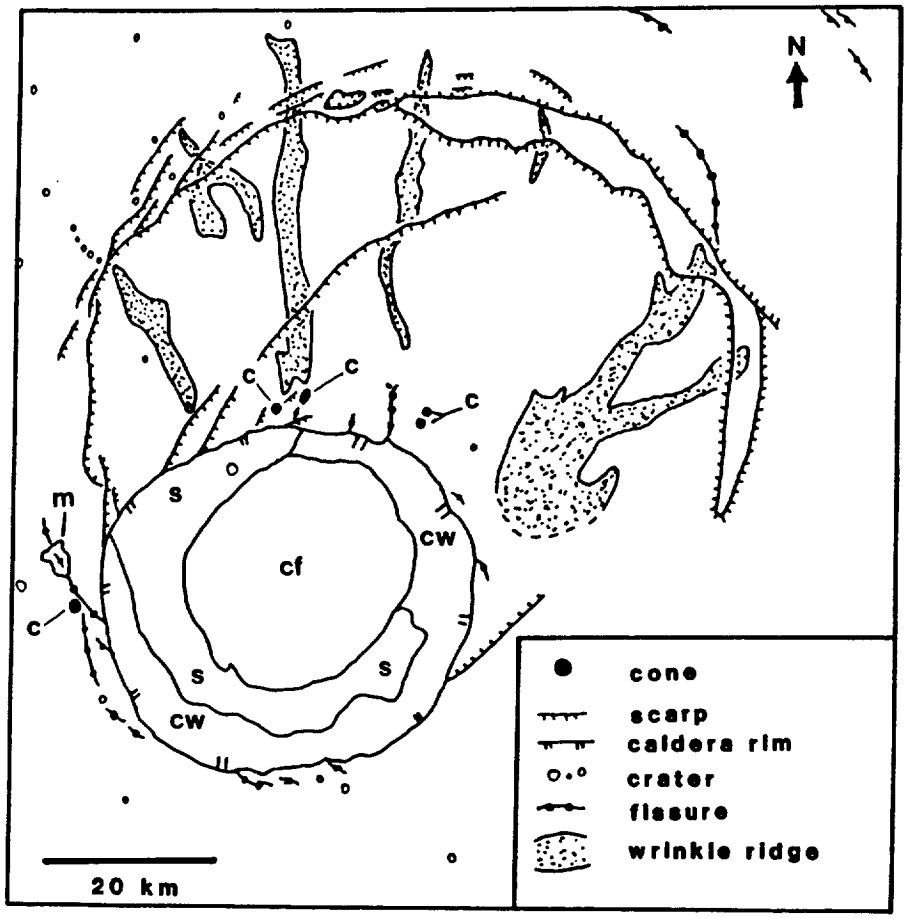

SAND ON MARS: DARK AEOLIAN DEPOSITS ON CRATER FLOORS RELATED TO REGIONAL WINDS. ***Kenneth S. Edgett and Philip R. Christensen,*** *Department of Geology, Arizona State University, Tempe, Arizona 85287.*

Intracrater dark features are common on Mars, especially on the floors of craters larger than ~25 km in diameter [1]. They typically occur on the predominant downwind side of the crater, and a number of them are composed of sand dunes [2-6]. The dark features, commonly termed "splotches" [7,8], are also apparently relatively free of incorporated fine dust [6] and coarse rocks [9]. All of the previous work that considered these features suggests that they have an aeolian origin, and that most may be composed of granulometrically unimodal deposits of sand-sized material. The purpose of the present study is to search for regional versus local differences in the properties of materials comprising the dark intracrater features; in order to make inferences concerning the nature and global distribution of martian sands.

The approach of this study involved: (1) examination of the highest resolution *Mariner 9* and *Viking Orbiter* photographs, in an effort to locate dunes, and (2) determination of the thermophysical properties of intracrater dunes, followed by the same for intracrater dark features with no visible duneforms. *Viking* Infrared Thermal Mapper (IRTM) 20 μm brightness temperatures and an assumed surface albedo of 0.15 were used to calculate thermal inertia. (The reader should note that a 0.15 albedo is a more realistic value than the 0.25 used to calculate thermal inertias presented in an earlier abstract [10]). A standard albedo of 0.15 was used because actual albedos for all of the dark intracrater features are not available. The IRTM data were constrained to avoid the effects of atmospheric dust, clouds, surface frosts, surface roughness, and surface emissivity. The best IRTM data for these purposes were taken at night (one reason for using an assumed albedo) and between L_S 344° to 125°. The resolution of the data were constrained, so that only data which lie exactly (or as close as possible) on the dark feature were used. Thermal inertia (expressed in units x 10^{-3} cal cm^{-2} $sec^{-1/2}$ $°K^{-1}$), at martian atmospheric pressures and temperatures, can be used to estimate effective particle size of unconsolidated materials [11,12]. This relationship is most useful for examining sand dunes, because they are the most likely martian feature which would be unconsolidated *and* have a unimodal grain size distribution which should be equal to the effective grain size determined by the thermal inertia-grain size relationship.

Compared to terrestrial dunefields, we would expect intracrater dunefields to have an effective particle size in the medium sand range (250 - 500μm, or 6.0 - 7.9 thermal inertia units) [13], or perhaps slightly larger [14]. The best IRTM data avialable for dunes is that of the large Hellespontus dunefields in the craters Kaiser, Rabe, and Proctor. The thermal inertias calculated for these are all ~8.0 (effective grain sizes ~ 550μm). The actual thermal inertias may be slightly less than 8.0, because the actual albedos for these dunes are closer to 0.13 rather than the standard 0.15 used to calculate thermal inertias from predawn data. Regardless of the actual albedo, it is clear that the thermal inertia of these dunes is consistent with an average particle size in the upper-medium or lower-coarse sand size range. Dunefields in the craters Wirtz (-48.5°, 25.6°) and Moreux (+42.1°, 315.5°) yield similar thermal inertias (8.4 and 8.3, respectively) and grain sizes.

Because the effective particle sizes indicated for the dunefields fall within a reasonable, expected range of grain sizes, we believe that the data for intracrater features that do not have visible duneforms also represent the actual effective particle sizes of those deposits. Figure 1 shows the range of thermal inertia values and effective grain sizes for 133 dark intracrater features in 11 geographic regions. The figure shows that there is a different mean thermal inertia for each region, each with a narrow range of variation in thermal inertia among individual dark features within the regions. The regions are identified on the basis of

overall regional albedo patterns [15] and the observed clustering of dark intracrater thermal inertia values reported here. The overall mean thermal inertia is about 8.4 (coarse sand, ~0.65 mm). The finest-grained intracrater deposits occur in Northern Arabia (NA), where the mean thermal inertia is 3.7 (very fine sand, ~0.07 mm), while the coarsest deposits occur in the Margaritifer Sinus (MS) region, where the mean is 13.7 (granules, ~ 2.5 mm). Many of the dark features are apparently composed of sand-sized particles, and might show duneforms when photographed at higher resolutions (most were photographed at resolutions > 150 m/pixel). Some of the deposits with high thermal inertias may be regions where there are barchan dunes with coarser interdune deposits; this is apparently the case for some of the dark deposits in the Oxia Palus region, where barchan dunes are seen in photographs with resolutions of less than 40 m/pixel.

Regions with the highest thermal inertia dark features correlate well with regions of high surface wind stress as predicted by the Mars General Circulation Model (GCM) [16, 17]. Greeley *et al.* (1989) [17] showed that there is a correlation between high surface wind stress and high rock abundance, suggesting that stronger winds remove fine particles from those regions [17, 18]. We speculate that the same may occur on the sandy, rock-free dark intracrater features. In regions where surface wind velocity is high, finer sands are winnowed out, leaving behind very coarse sand and granules. In Northern Arabia, where the dark features effectively consist of very fine sands, the regional winds are correspondingly low. Alternatives include the barchan dunes with coarse interdune explanation, and the possiblity that the coarser sands simply occur nearer to their source.

REFERENCES: [1] Arvidson, R.E. (1974) *Icarus, 21*, 12-27. [2] Cutts, J.A. and R.S.U. Smith (1973) *J. Geophys. Res., 78*, 4163-4196. [3] Breed, C.S. (1977) *Icarus, 30*, 326-340. [4] Peterfreund, A.R. (1981) *Icarus, 45*, 447-467. [5] Thomas, P. (1982) *J. Geophys. Res., 87*, 9999-10008. [6] Thomas, P. (1984) *Icarus, 57*, 205-227. [7] Sagan. C. *et al.* (1972) *Icarus, 17*, 346-372. [8] Sagan, C. *et al.* (1973) *J. Geophys. Res., 78*, 4163-4196. [9] Christensen, P.R. (1983) *Icarus, 56*, 496-518. [10] Edgett, K.S. and P.R. Christensen (1990) *Lunar Planet. Sci. XXI*, 313-314. [11] Kieffer, H.H. *et al.* (1973) *J. Geophys. Res., 78*, 4291-4312. [12] Kieffer, H.H. *et al.* (1977) *J. Geophys. Res., 82*, 4249-4292. [13] Ahlbrandt, T.S. (1979) *in* McKee, E.D. (ed), *A Study of Global Sand Seas, U.S.G.S. Prof. Paper 1052*, 21-51. [14] Greeley, R. and J.D. Iversen (1985) *Wind as a Geological Process on Earth, Mars, Venus, and Titan*, Cambridge Univ. Press, 333p (esp. see p. 70). [15] Pleskot, L.K. and E.D. Miner (1981) *Icarus, 45*, 179-201. [16] Pollack, J.B. *et al.* (1981) *J. Atmos. Sci., 38*, 3-29. [17] Greeley, R. *et al.* (1989) *Lunar Planet. Sci. XX*, 359-360. [18] Skypeck, A. (1989) *M.S. Thesis*, Arizona State Univ., Tempe, Arizona.

FIGURE 1. Regional variation of intracrater dark feature thermal inertia. The points show the average thermal inertia of dark intracrater deposits in each region shown on the map. The bars represent one standard deviation from the mean. Numbers to the right of the bars indicate the number of data points included in each region. Grain sizes are based on the standard Wentworth scale, the relationship between thermal inertia and grain size is best explained by Kieffer *et al* (1973) [11]. One region not depicted on the map, SP, includes dunes of the south polar region, between latitudes -65° and -75°, and longitudes 145° to 250°. There are a number of uncertainties in the south polar dunes data, and they may not be representative of the acutal thermal inertias.

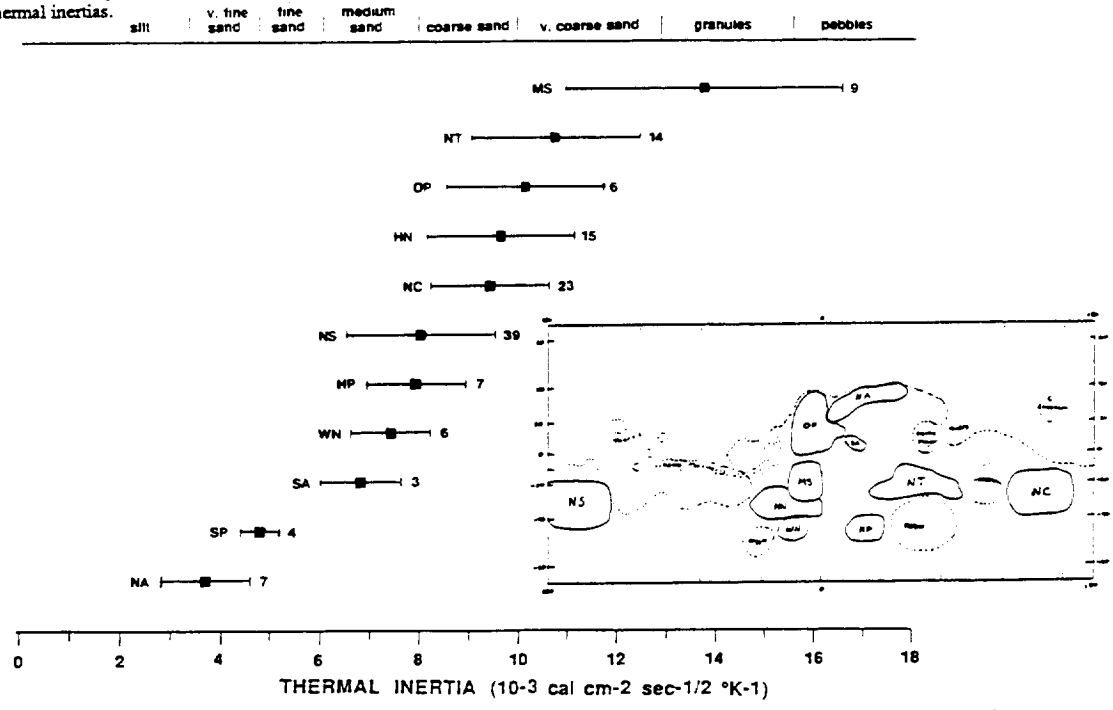

THE ARSIA MONS-OTI FOSSAE THERMAL ANOMALY: A REGION WITH A HIGHER THERMAL INERTIA THAN THE REST OF THARSIS.

Kenneth S. Edgett, *Department of Geology, Arizona State University, Tempe, AZ 85287; and* ***James R. Zimbelman,*** *Center for Earth and Planetary Studies, National Air and Space Museum, Washington, DC 20560.*

Global mapping of the thermal properties of the martian surface have shown that the Tharsis region is largely covered by low thermal inertia materials; interpreted to be very fine (clay and silt-sized), unconsolidated particles which may occur in accumulations up to 2 meters thick [1-4]. Tharsis, Arabia, and Elysium are considered by Christensen [4] to be regions of net dust deposition following annual dust storms; and net dust transport is thought to switch from south->north to north->south approximately every million years.

Nearly the entire Tharsis region appears to have a covering of dust; this is seen even in the highest spatial resolution *Viking* thermal infrared data [5-7]. One area in Tharsis, located on the plains adjacent to the east-southeastern margin of Arsia Mons, has a consistently higher thermal inertia than the rest of Tharsis. This region, near the Oti Fossae fracture system, covers approximately 15,700 sq. km. The anomaly was first reported in an analysis of early data from the *Viking* Infrared Thermal Mapper (IRTM)[8], an infrared scanning radiometer sensitive to five mid-IR bands centered on 7, 9, 11, 15, and 20 μm plus a visible/near-IR band from 0.3 to 3.0 μm [9]. Kieffer *et al.* [8] reported that this region east of Arsia Mons is cool during the afternoon and warm in the nighttime. The thermal anomaly appeared in subsequent moderate resolution thermal maps [1,2,10], but none attempted to explain the feature. The Oti Fossae thermal anomaly also appears in high resolution (3-5 km) IRTM data [5] and in a high resolution (2-3 km) *Phobos 2* Thermoscan image obtained on 26 March 1989 [11,12]. It is clearly a surface phenomenon rather than an atmospheric anomaly.

Figure 1 is a sketch of the anomalous region. The shaded area corresponds to a region of slightly lower albedo than its surroundings. We were not able to obtain a reliable figure for the albedo, as daytime observations in the region are commonly hampered by clouds and haze. The contoured track in Fig. 1 is a high resolution map of thermal inertias (units x 10^{-3}cal $cm^{-2}sec^{-1/2}K^{-1}$) calculated from predawn 20μm brightness temperatures measured by the *Viking 1* IRTM (orbit-sequences 461-5 and 500-1) during Southern Summer after the 1977 dust storm. The highest thermal inertias measured are around 8.0. Application of Christensen's [13,14] two-component block abundance model to the data gives a figure of ~ 0% blocks for all points in the high resolution sequences: on the anomaly, on the adjacent plains, and on the Arsia Mons shield.

Viking photographs (Table 1) of the anomalous region do not reveal anything unusual about the area. The region appears as a darker spot relative to its surroundings only in the *Viking* images 641A85, 52A07, and 52A09; the other images are hazy. The dark spot does not appear to be as dark as the upper slopes of Arsia Mons. It is

FIGURE 1: Sketch Of The Eastern Arsia Mons Thermal Anomaly

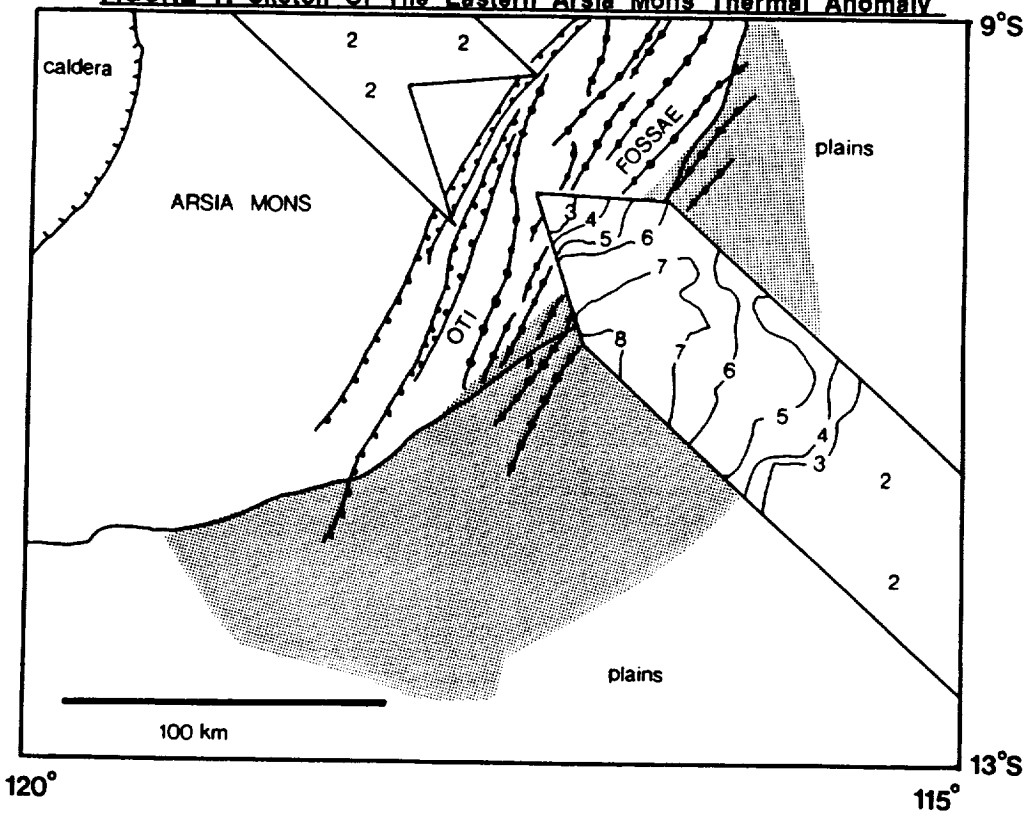

possible that dust in the atmosphere causes the apparent difference between the dark shield surface seen at high elevations relative to the more hazy, dark anomalous feature which occurs at a lower elevation. There are no *Mariner 9* B-frame images of this region.

Zimbelman [15] observed that the thermal properties of the Oti Fossae anomaly are similar to surfaces on Solis Planum to the southeast. Assuming a model where there is cyclic removal and deposition of dust on a scale of one million years [4], both the anomalous surface and the surfaces of Solis Planum could be made up of indurated soils from a previous climatic cycle. Zimbelman [15] suggested that the Oti Fossae anomaly is a "window" through the present dust cover. To test the "window" hypothesis and comparisons with Solis Planum, we chose two 0.1°x 0.1° latitude/longitude bins, each along the high resolution track in Fig. 1, and each with a thermal inertia of 7.9. One location is in the anomalous region centered at -10.8°,116.9°, the other on Solis Planum at -23.3°, 99.8°. We calculated emissivities for the 11 and 20 μm bands, assuming that the 7 μm brightness temperature closely approximates the surface kinetic temperature [13,16]. The 20 μm emissivities were both 0.94, while the 11 μm emissivities were different by 0.04 (0.93 and 0.97, respectively). This is not conclusive evidence that the surfaces at these two locations are made up of similar-composition materials, but neither does it weaken the proposed relationship.

There are three possible explanations for the Oti Fossae region thermal anomaly which are consistent with the observations. The area is definitely a region where there is no net dust deposition. It may be either an indurated soil (commonly termed "duricrust" in the literature [17,18]), a deposit of unconsolidated sand, or a surface where the dust cover is very thin, so that an underlying consolidated surface (bedrock or "crust") contributes to the thermal behavior of the region. Because the region appears somewhat darker than its surroundings, this would argue against the third hypothesis, since only a thin coating of dust is needed to change the surface albedo.

Under martian atmospheric pressure and temperature conditions, thermal inertia ($I = (kpc)^{1/2}$) is strongly dependent upon thermal conductivity (k) [19,20], and both are closely related to unconsolidated particle size [20]. The thermal inertias observed for the Oti Fossae anomaly (5.0 to 8.0) are consistent with a surface of unconsolidated sand. If the anomaly results from sand, it may be difficult to explain the zonation of thermal inertias (Fig. 1), indicating grain sizes increasing toward the center. A large field of sand would explain the presence of the anomaly in Tharsis; saltating grains can remove dust from sand sheets [21]. To determine if the anomalous region is a sand sheet will require images with very high resolution to search for duneforms.

A surface composed of partially cemented fine particles might also be consistent with the observed thermal inertias [*eg.* 22] and low block abundance. Variations in thermal inertia may occur for a constant particle size (*eg.* "dust") if the thermal conductivity can be increased by bonding the grains [*eg.* 18,23]. If the anomalous feature results from intergranular bonding of dust, the zonation of thermal inertias might result if either: (1) the feature results from wind stripping recently accumulated dust off the surface, where removal has been most complete toward the center, or (2) the zonation results from differing degrees of bonding between grains, suggesting that rather than a "window" to a past soil surface, the region could be undergoing cementation at the present. Testing the "duricrust" hypothesis might be more difficult than testing for sand, since it would likely require *in situ* observations for conclusive results. On the other hand, a lack of duneforms might be construed as further evidence for the crust hypothesis. The *Mars Observer* Thermal Emission Spectrometer should be able to detect the composition of the anomalous region, and could provide additional information about its surficial properties.

TABLE 1: *Viking* Photographs Of The Anomalous Region

Frame	resolution (m/pixel)	Notes
52A07,09	175 m/p	dark spot visible, despite some clouds
210A47-50	89 m/p	hazy, spot not visible
641A85	287 m/p	spot visible as mapped in Fig. 1
42B30,46	140,170 m/p	hazy, spot not visible

Notes and References: [1] Kieffer, H.H. *et al.* (1977) *J. Geophys. Res., 82,* 4249-4291. [2] Zimbelman, J.R. and H.H. Kieffer (1979) *J. Geophys. Res., 84,* 8239-8251. [3] Palluconi, F.D. and H.H. Kieffer (1981) *Icarus, 45,* 415-426. [4] Christensen, P.R. (1986) *J. Geophys. Res., 91,* 3533-3545. [5] Edgett, K. and J.R. Zimbelman (1986) *Papers Presented 2nd Ann. Summer Intern Conf., L.P.I.,* Houston, L.P.I. Contrib. 602, 9-11. [6] Zimbelman, J.R. (1986) *Trans. Am. Geophys. U. (EOS), 67,* 1074. [7] Zimbelman, J.R. *et al.* (1987) *Lunar Planet. Sci. XVIII,* 1128-1129. [8] Kieffer, H.H. *et al.* (1976) *Science, 194,* 1346-1351. [9] Chase, S.C. *et al.* (1978) *Appl. Opt., 17,* 1243-1251. [10] Christensen, P.R. and M.C. Malin (1989) in (M. Zuber *et al.*, eds.) *Planetary Geosciences-1988, NASA SP- 498,* 6-7. [11] Crumpler, L.S. *et al.* (1990) In *Abs. Pres. to MEVTV Workshop on the Evolution of Magma Bodies on Mars,* San Diego, CA, p. 16-17. [12] Selivanov, A.S. *et al.* (1989) "Phobos Shadow On Surface of Mars," *Papers Presented to the Phobos 2 Conference, Paris* . [13] Christensen, P.R. (1982) *J. Geophys. Res., 87,* 9985-9998. [14] Christensen, P.R. (1986) *Icarus, 68,* 217-238.[15] Zimbelman, J.R. (1984) PhD Diss., Arizona State Univ., Tempe, AZ, see p. 232 (reprinted in *Adv. Planet. Geol., NASA TM-88784* (1986), see p. 516). 16] Christensen, P.R. (1984) *Lunar Planet. Sci. XV,* 150-151. [17] Ditteon, R. (1982) *J. Geophys. Res., 87,* 10197-10214.. [18] Jakosky, B.M. and P.R. Christensen (1986) *J. Geophys. Res., 91,* 3547-3559 [19] Neugebauer, G. *et al.* (1971) *Astron. J., 76,* 719-728. [20] Kieffer, H.H. *et al.* (1973) *J. Geophys. Res., 78,* 4291-4312. [21] Sagan, C. and J.B. Pollack (1969) *Nature, 223,* 791-794. [22] Presley, M.A. and R.E. Arvidson (1988) *Icarus, 75,* 499-517. [23] Kieffer, H.H. (1976) *Science, 194,* 1344-1346.

PHOTOMETRIC TECHNIQUES FOR LANDER SITE CERTIFICATION. Nicholas D. Efford, IEBS, Environmental Science Division, University of Lancaster, Lancaster LA1 4YQ, U.K.

In view of the need to safeguard wideranging scientific objectives and a considerable investment of human effort and funding, the certification of an acceptable landing site is of paramount importance in any spacecraft mission involving the deployment of an unmanned lander probe. In the case of Viking, boulders greater than 0.22 m in size represented potentially fatal hazards, yet features smaller than roughly 100 m across could not be recognised in the images used for site certification [1]. As even a cursory examination of the Viking Lander images will illustrate, the techniques employed to circumvent this problem, namely the extrapolation of visible detail down through more than two orders of magnitude coupled with the utilisation of Earth-based radar roughness measurements [2], are of limited value; the assumptions inherent in the former may be unjustified, whilst the latter suffers from poor spatial resolution and ambiguities in interpretation, in that, for example, the penetrating character of electromagnetic radiation may result in the detection of sub-surface roughness not necessarily indicative of unduly hazardous surface topography. Site reconnaissance at extremely high (i.e. 1 m pixel^{-1} or better) resolution, such as that recommended for future Mars missions [3], is a direct yet in many ways impractical solution, given optical system design technicalities and the number of images that must be acquired to adequately cover the areas targetted by landing ellipses. There is thus a need for economical methods of hazard detection that operate at sub-pixel scales and make use of existing, commonly-employed spacecraft instrumentation, such as the imaging system itself.

Pixel-Scale Feature Detection. Positive-relief features on a flat plane will in general have a bright sunward-facing side abutting a darker side, which is tilted away from the Sun and possibly in shadow, given a sufficiently high incidence angle. The net effect on pixel reflectance will be minimised if the bright and dark sides of the feature are wholly contained within the projected area of a single pixel. It is statistically likely, however, that some objects will be favourably positioned so as to produce a detectable signature in the image, namely one or more anomalously bright pixels immediately adjacent to one or more anomalously dark pixels. This signature has been identified in a small subregion of a Viking Orbiter frame containing the site of the Mutch Memorial Station, and has been interpreted as signifying the presence of a boulder roughly 10 m across [4].

To determine the limits of detectability for such anomalies, a digital terrain model (DTM) was constructed by the emplacement of randomly-located obstacles, each of uniform size with a parabolic or conic cross-section. An initial synthetic image was generated from the DTM under near-optimum conditions of viewing and illumination (zero emergence angle e and moderate-to-high incidence angle i) by the method described in [5], and this was artificially degraded by the enlargement of pixel size to produce images with a range of spatial resolutions. Figure 1 plots the standard deviation of imaging pixel DN against image resolution for a DTM populated by 40 cones with base radii of 1.5 m and heights of 2 m. A Lommel-Seeliger surface scattering law with $i = 60°$ was assumed. The horizontal dashed lines indicate points at which the anomaly becomes statistically insignificant, for a given error in pixel DN. Clearly, if unrealistically-extreme aspect ratios are ignored, this technique is of little use for obstacles smaller by a factor of two or more than the size of an imaging pixel.

Sub-pixel Scale Feature Detection. Given suitable images of the potential landing site obtained under a variety of viewing and illumination conditions, it is possible to fit Hapke's bidirectional reflectance equation [6] to photometric measurements in order to derive an estimate of $\bar{\theta}$, a parameter generally corresponding to the mean slope angle of unresolved surface roughness. The principal requirement is the availability of high phase angle data, and since survey images are likely to be acquired at or near $e = 0°$, this translates in practice to the requirement that the maximum value of i is large. Under such conditions, the presence of unresolved shadows will darken a pixel in a manner quantified by $\bar{\theta}$. The relationship between this parameter and the probability of a successful landing was investigated by using the previously-described synthetic topography and modelling the photometric properties of surface material with Hapke's equation, setting $\bar{\theta} = 0°$ and the remaining parameters to arbitrary values. Average DTM reflectance was computed for a range of incidence angles, and the resulting data were used to solve for $\bar{\theta}$ only, as described in [5].

Figure 2 plots $\bar{\theta}$ against both the population of hazardous obstacles, n, and the probability of success, P_{succ}, the latter being determined for features with a circular base of radius r in a square pixel of size x by the equation $P_{succ} = 1 - (n\pi r^2/x^2)$. Here, r = 1.5 m and x = 50 m. A clear relationship between $\bar{\theta}$ and P_{succ} exists, but an observed photometric roughness of 15° may imply probabilities of either 96% or 84%, depending on the height of the obstacles. The usefulness of this technique will therefore be somewhat limited without contraints on the morphology and size distribution of obstacles at the proposed site. In the case of Mars, it might be possible (though not necessarily appropriate) to derive these constraints from Viking Lander images. More practical limitations result from the accuracy with which $\bar{\theta}$ can be estimated from inevitably sparse orbital imaging data; restricted phase angle coverage or the assumption of incorrect Hapke parameters in constrained fits of $\bar{\theta}$ can have a serious effect [7]. Recent photometric studies of dust deposits in the vicinity of the Mutch Memorial Station [8] provide Hapke parameter estimates that might be applicable in those cases where it proves necessary to assume values for all parameters other than $\bar{\theta}$, though further careful investigation of the photometric properties of martian terrain is evidently required.

In conclusion, neither technique can be expected to provide accurate quantitative estimates of landing success probabilities, given the large number of potential sources of error that exist. However, it is envisaged that both could usefully supplement existing methods; the cumulative application of a wide range of techniques can only improve the reliability of the certification procedure and hence the likelihood of a successful landing on Mars, or for that matter, other bodies in the solar system.

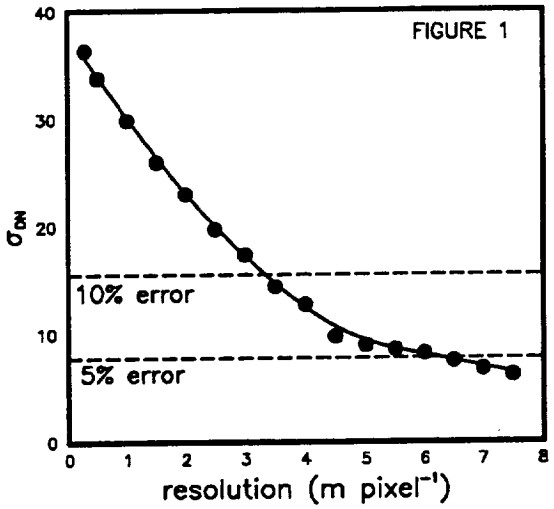

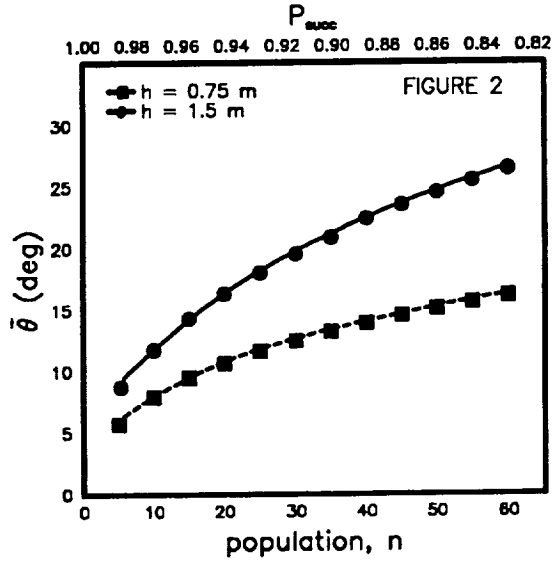

Acknowledgements: The author was supported during the course of this work by a SERC research studentship.

REFERENCES: [1] Soffen, G.A. *et al.* (1977) *J. geophys. Res.* **82**, 3959–3970. [2] Masursky, H. & N.L. Crabhill (1976) *Science* **193**, 809–811. [3] Henderson, B.W. (1989) *Aviation Week & Space Technology* **131**, no. 5, 85–94. [4] Wilson, L. *et al.* (1984) *Lunar Planet. Sci.* **XV**, 920–921. [5] Helfenstein, P. (1987) *Icarus* **73**, 462–481. [6] Hapke, B. (1984) *Icarus* **59**, 41–59. [7] Efford, N.D. (1989) Ph.D. thesis, in preparation. [8] Arvidson, R.E. *et al.* (1989) *J. geophys. Res.* **94**, 1573–1587.

DETERMINATION OF SPECTRAL UNITS IN THE SYRTIS MAJOR-ISIDIS PLANITIA REGION FROM PHOBOS/ISM OBSERVATIONS;

S. Erard[1], J-P. Bibring[1], J. F. Mustard[4], Y. Langevin[1], M. Combes[2], J.W. Head[4], S. Hurtrez[3], C. Sotin[3].
[1]Institut d'Astrophysique Spatial, Orsay, 91406, France; [2]Departement de recherches spatiales, Observatoire de Paris-Meudon, France; [3]Laboratoire de Géophysique, Université de Paris-Sud, Orsay, 91405, France; [4]Department of Geological Science, Brown University, Providence, R.I.

Introduction: On March 1st 1989, the ISM spectrometer on the Phobos 2 probe observed the Syrtis-Isidis domain. This window contains very different units including Isidis Planitia, its heavily cratered rim, and the dark Syrtis Major shield. It provides an opportunity to observe the crustal dichotomy in the eastern hemisphere. The domain lies between longitudes 240°W and 310°W, and latitudes 2°N and 9°N (Fig. 1). The image is made of 25 x 120 pixels (3000 x 450 km^2), each one (20 x 20 km^2) being a set of 128 spectral measurements ranging from 0.76 to 3.16 μm (1).
Data correction process is the following : 1) Dark current substraction, 2) Detector temperature correction, 3) Gain correction, 4) Spectral orders overlap removal, 5) Division by the transfert function, and 6) Division by a solar spectrum, taking into account the Sun-Mars distance at this date. Some instrumental effects remain, weak enough to allow mineralogic identifications (2,6).

First results : Three simple criteria bearing the most part of the spectral variance were used for quick-look analysis (3). Brightness (Fig. 2) accounts for more than 80% of this variance, the instrument having observed two very different types of terrains. In particular, Syrtis Major is known to be one of the darker parts of Mars. Brightness (Fig. 2) ranges from 0.1 to 0.35, varying by a factor of three between Isidis and Syrtis. In this case, the brightness is very close to albedo, slopes being relatively weak. Hydration was estimated by using the depth of the 2.9 μm H_2O absorption band. The spatial distribution is close to that of the brightness, opposing mainly a very dry Syrtis (25% absorption) to a very hydrated Isidis (40% absorption). Reddening (ratio of intensities at 2.39 μm and 1.79 μm) has a similar spatial distribution. It also exhibits a second order discrepancy within Syrtis. The general slope in the spectra is partly due to atmospheric dust.

Methods used to determine the spectral units : In order to use the total spectral information, four principal component analysis (PCA) have ben carried out, one for each set of 32 channels (odd and even, first and second orders). This allows us to avoid major discrepancies in viewing directions. Rough atmospheric corrections are performed with a simple atmospheric spectrum from the Pavonis high resolution track combined with a linear model and based on the strengh of the CO_2 2 μm absorption band (4). Since brightness variation is the major information, each quarter-spectrum has been divided by its own mean value in order to see second order features that define five main units (Fig. 3). Another method has been used to define the different spectral units. Two reference spectra are chosen respectively in the darkest area (Syrtis) and in the brightest area (Isidis). The location of the reference spectra is taken in a homogeneous domain. For each pixel, the spectrum is fit as a linear combination of the two reference spectra. For each pixel, the variance between the theoretical spectrum and the observed spectrum is determined. The spatial distribution of both brigthness and residual variance allows the definition of five units as those defined with the previously described method.

Results: Results obtained with the odd and even channels are very consistent : a strong contrast between hydration and a broad absorption band centered at 2.3 μm, attributed to high-Ca pyroxenes; another contrast in the second order between two silicate bands centered around 0.9 and 1.1 μm. Five domains can be defined, which are spatially consistent with observation of images of the surface of Mars. Isidis Planitia (domain 1) bright and hydrated with poor mineralogic features, except an absorption band at 0.9 μm, seems to be covered with a thick dust layer. A smooth plain in the SE, crossing the heavily cratered rim in a NW-SE direction, exhibits similar features. The cratered rim of Isidis in the South (domain 2) and Arabia (domain 3) in the NW corner are a little drier, and exhibit a weak absorption band at 2.3 μm. The Syrtis Major region seems to be free from dust, much darker and drier, with strong absorption features corresponding to mafic minerals, in

particular around 1 μm. The Eastern part of Syrtis Major (domain 4) is bluer and drier than the Western part (domain 5). Also, the shape and position of the 1 μm band are different between these two domains within Syrtis. Differences in slopes is partly due to surface materials, since albedo is about the same, and possibly related to a thin weathered coating (6). In Syrtis Major, several smaller spatial features of particularly interest are observed near the region's topographic crest. Further interpretation of ISM spectra in terms of mineralogy within each of the previously defined units is done in the companion paper (5). A more detailed study on this region and the Valles Marineris domain was carried through (6).

References : (1)Bibring et al., *Nature 341, 6242,591-592*, 1989 (2)Bibring et al., *Lunar Planet. XXI*, 1990 (3)Erard et al., *DPS*, 1989 (4)Bibring et al., *Proceedings of Lunar Planet. XX*, 1990 (5)Mustard et al., this volume, 1990 (6)Erard et al., submitted to *Proceedings of Lunar Planet. XXI*, 1991.

Figure 1. Map of depth of CO_2 2 μm absoption band correlated with topography, and location of the window.
Figure 2. Brightness, computed as a geometrical mean of intensities at 0.99, 1.07, 1.10 μm
Figure 3. Detailed synthetic map with the five spectral units determined from multifactorial analysis. Some sub-units are delimited, with the shading of the principal unit.

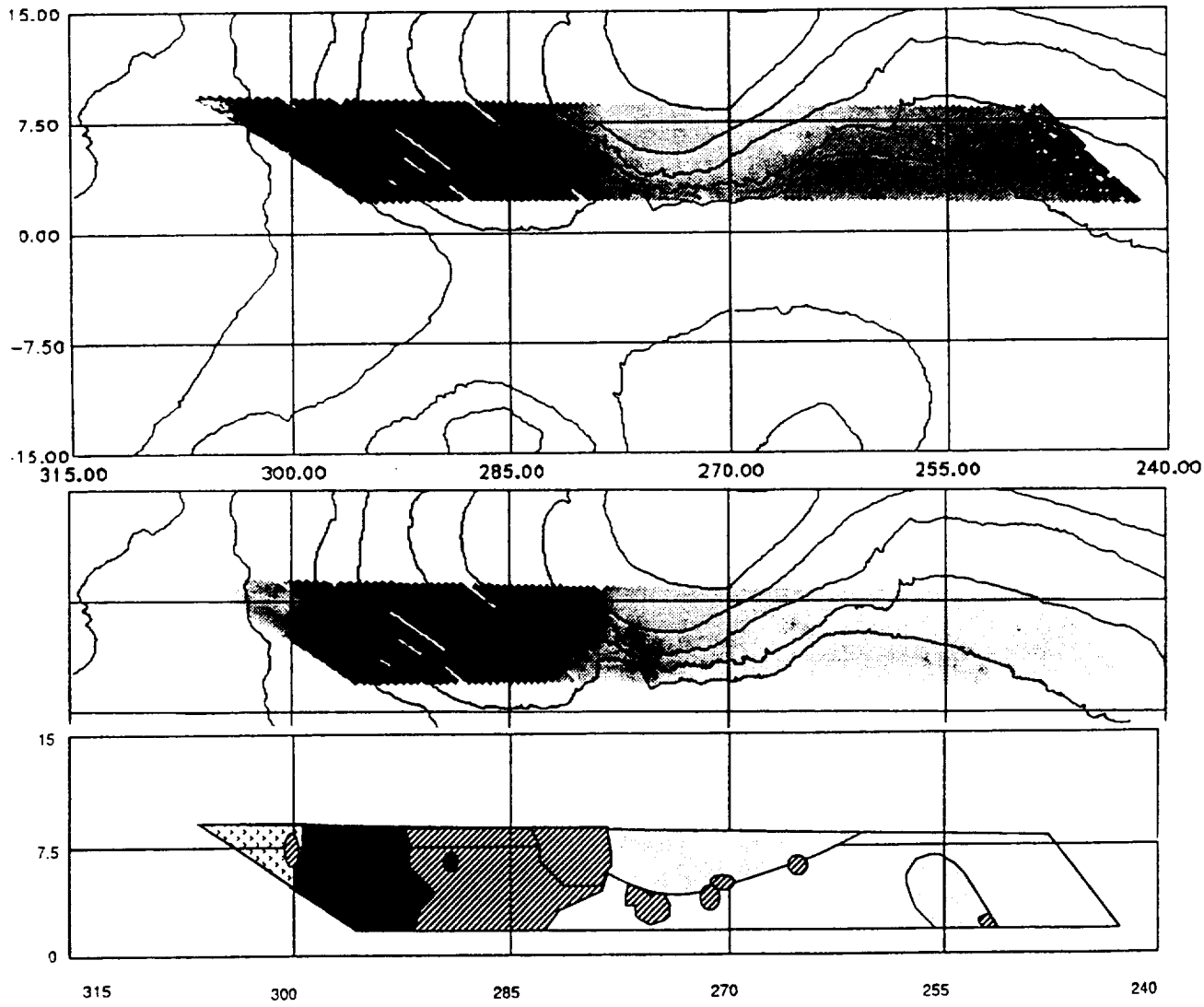

HEAT FLOW vs. ATMOSPHERIC GREENHOUSE on EARLY MARS. Fraser P. Fanale and Susan E. Postawko, Planetary Geosciences Div., Univ. of Hawaii, 2525 Correa Rd., Honolulu, HI 96822

Long term climate change on Mars is suggested by an apparent difference in the erosional style exhibited by the ancient cratered terrain as opposed to terrain of later origin. In particular, the morphology and distribution of valley networks on Mars clearly indicates a difference in erosional style ~3.8 billion years ago versus mid-to-late martian history. Liquid water was certainly involved in network formation, although sapping processes rather than rainfall seem indicated. Two major factors could have contributed toward making early conditions more favorable to formation of valley networks:

First, it has been argued (1) that higher internal regolith temperatures, associated with a much higher heat flow 3.8 AE, would cause groundwater to be closer to the surface then than at present. Higher heat flows are expected early in Mars' history primarily because of dissipation of the original heat of formation, although a higher rate of production of radiogenic heat is also a factor.

Second, if enough CO_2 is in the atmosphere, surface temperatures could be raised, due to an increased atmospheric greenhouse effect, to near the freezing point of water despite a weak early sun - at least at the equator and for the most favorable part of the orbital and axial cycle. Current greenhouse models indicate that CO_2 surface pressures of between about 0.75 and 5 bars are needed to raise the surface temperature on early Mars to the freezing point of water. Only slightly lower pressures characterize greenhouse warmings that are 10 to 20° K cooler.

In fact, the effectiveness of both these mechanisms is dependent on a high early heat flow: In the case of the atmospheric greenhouse, this is because the atmospheric mean residence time (M.R.T.) of CO_2 in the presence of fluvial activity is believed to be much shorter than the span of time over which network formation occurred. Thus, the atmospheric P_{CO2} would have been dependent almost exclusively on the recycling time for regolith carbonate rather than the instantaneous supply of juvenile CO_2. Both of these parameters can be quantitatively related to the heat flow. The depth to the water table, ΔZ_{273}, also depends on internal regolith temperatures. For a given regolith conductivity, k, the temperature at any depth is determined by the heat flow, which determines the gradient, $\partial T/\partial Z$, and the surface temperature, T_S.

We have derived a quantitative relationship between the effectiveness of an atmospheric greenhouse and internal heat flow in producing the morphological differences between early and later martian terrains. Our derivation is based on relationships previously derived by other researchers (2). Thus, while the validity of our derivation is dependent on the validity of these previously derived relationships, no new assumptions or mathematical relationships are necessary - merely algebraic manipulation of relationships already in the literature.

Our reasoning may be stated as follows: The CO2 mean residence time in the martian atmosphere, although not well known, is almost certainly much shorter than the total time span over which early climate differences are thought to have been sustained . Therefore recycling of previously degassed CO2 quickly becomes more important than ongoing supply of juvenile CO2 . If so, then the atmospheric CO2 pressure - and therefore the surface temperature - may be approximated mathematically as a function of the total degassed CO2 in the atmosphere plus buried material and the ratio of the atmospheric and regolith mean residence times. The latter ratio can also be quantitatively expressed as a function of heat flow . Hence, it follows that the surface temperature may be expressed (given assumptions as to regolith conductivity) as a function of heat flow and the total amount of "available" CO_2. However, the depth to the water table - again assuming the same regolith conductivity - can simultaneously be expressed as a function of heat flow and the surface temperature (the boundary condition). Therefore, for any given values of total available CO_2 and regolith conductivity, there exist coupled independent equations which relate heat flow, surface temperature and the depth to the water table. This means that we can now derive <u>simultaneous</u> values of surface temperature and the depth to the water table for <u>any</u> value of the heat flow. We utilize the derived relationship for two purposes: 1) To evaluate the <u>relative</u> importance of the atmospheric greenhouse effect and the internal regolith thermal gradient in producing morphological changes for <u>any</u> value of the heat flow and

2) to assess the absolute importance of each for values of the heat flow which are thought to be reasonable on independent geophysical grounds.

Figure 1 illustrates that for a given amount of total available CO_2, regolith conductivity and atmospheric M.R.T., the relative roles of internal heat flow and atmospheric greenhouse are inextricably interlocked. Figs. 1a and 1b are for a case of a cool early sun, favorable orbital situation, and an equatorial site (after ref. 2). The mean residence time of atmospheric CO_2, and regolith conductivity are the same in both figures. The figures show surface temperature (T_S) as a function of depth to the water table (z). The numbers in parentheses indicate heat flow in mW m^{-2}.

In Figure 1a, total CO_2 = 3.5 bars. Note that the internal heat flow predicted by (1) for ~3.8 AE ago, that is ~150 mW m^{-2}, is more than sufficient to recycle enough CO_2 to keep surface temperature at the freezing point because we have assumed so much total CO_2. In this case, the surface greenhouse effect plays a dominant role. However, if one considers that a water table depth of < 350 m is sufficient to permit widespread sapping, it is clear that the internal thermal gradient also plays a major role in widening the latitudes and time bands in which sapping would be prevalent. Thus this case is not very different either in assumptions or result from those discussed by (2).

In Figure 1b total CO_2 is only one bar. This case is important because in many plausible versions of the early Mars volatile inventory it is entirely possible that the total available CO2 at 3.8 AE might have been only a bar, or even less. In this case we find that the atmospheric greenhouse effect plays almost no role because the low total CO_2 abundance requires incredibly fast recycling in order to keep any significant abundance in the atmosphere. Thus for plausible values of earlier heat flow, the surface temperature changes by only a few degrees. On the other hand, the early heat flow produces an enormous direct effect on the depth to the 273K isotherm despite the near constancy of surface temperature; at Q = 30 mW m^{-2} the depth is over a km, but at Q = 100 mW m^{-2} it is less than 300 m and near the critical depth suggested by (1).

All these calculations are sensitive to the values chosen for the (unknown) regolith conductivity, the CO_2 atmospheric mean residence time, and especially total CO_2 inventory assumed. Thus it is important to explore the sensitivity of the conclusions to the values chosen. Although our exploration of the parametric space has been limited, the qualitative characteristics of the system are apparent.

We find that if the total available CO_2 has always been ~4 bars or more, then the atmospheric greenhouse effect can easily account for the change in erosional style, and the primary role of the heat flow is to raise ground water temperatures. This result is in keeping with the earlier results of (2). On the other hand, if the total CO_2 were only ~1 bar, the atmospheric greenhouse effect does not raise the surface temperature by more than a few degrees, but for plausible values of regolith conductivity the change in internal gradient accompanying higher early heat flow can still easily decrease the water table depth by a large factor, from well over a kilometer to less than 350 m, enabling network formation at 3.8 AE.

REFERENCES: (1) Squyres, 1989. Fourth International Conf. on Mars, Tucson, AZ. (2) Pollack et al., 1987. Icarus *71*, 203-224. (3) Schubert et al., 1979. Icarus *38*, 192-211.

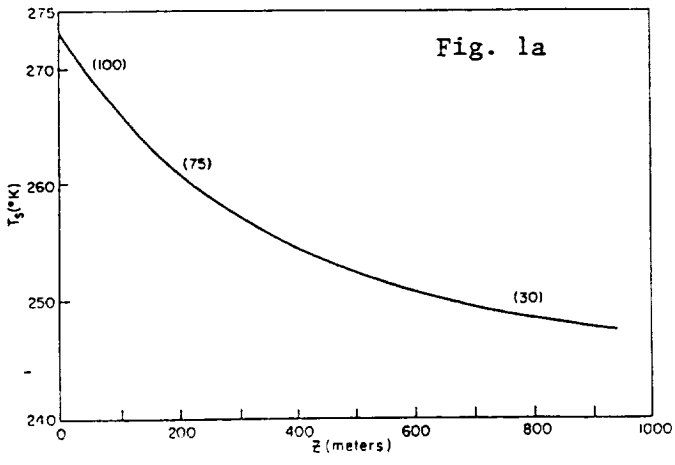

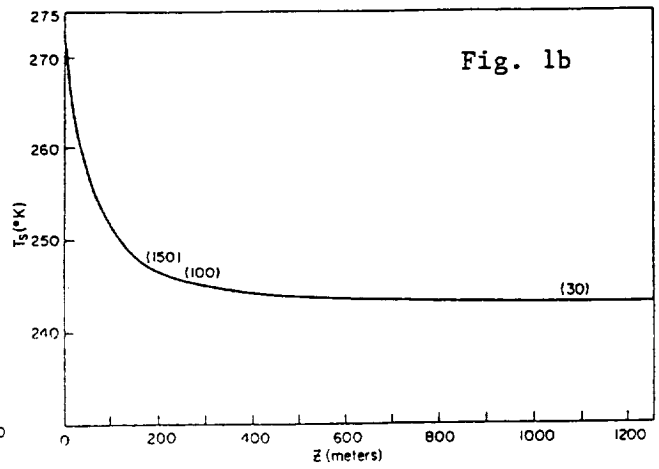

ANALYSIS OF POORLY CRYSTALLINE CLAY MINERALOGY: NEAR INFRARED SPECTROMETRY *VERSUS* X-RAY DIFFRACTION

William H. Farrand and Robert B. Singer, Planetary Image Research Laboratory, University of Arizona, Tucson, AZ 85721

Clay minerals are arguably the most abundant group of minerals at the Earth's surface, occurring in hydrothermal alteration zones and a host of sedimentary environments. On Mars, the existence of clay minerals has been hotly debated; their existence or absence has important implications for the type of surface processes which have acted through that planet's history and should provide clues to past climate. Given the importance of clay minerals, it is important to know the capabilities and limitations of various analytic methods that can detect and identity clay minerals. This study makes some direct comparisons between two such laboratory analytic methods, X-ray diffraction (XRD) and near infrared (NIR) reflectance spectrometry.

Before the advent of XRD demonstrated the existance of crystalline structure in clays minerals, they were regarded as being composed of amorphous phases [1]. XRD studies showed that any given clay specimen can be thought of as lying somewhere on a continuum between a highly-crystalline end member and an amorphous endmember. Some of the debate about the existence of "clays" vs. "palagonites" on Mars is semantic, since for different researchers these names imply different regions of this continuum. Nevertheless, the degree of crystallinity of a clay is closely related to its formation conditions, information which we very much wish to decipher.

The data for the comparison of techniques presented here are from an ongoing study of basaltic hydrovolcanism on Earth, with applications to Mars. Hydrovolcanism, the explosive interaction of magma with surface or near surface water [2], commonly produces tuff rings and tuff cones when the magma is basaltic in composition. The alteration product of basaltic glass (sideromelane) is termed palagonite, and a tuff in which the sideromelane has been largely altered to palagonite is called a palagonite tuff. The clay size-fraction (< 2 μm) of such tuffs has, at best, only poorly crystalline clays, and therefore lies toward the "amorphous" end of the continuum discussed above.

For this study, samples from two tuff rings and one tuff cone were analyzed. The tuff rings were Ubehebe Crater, CA and Zuni Salt Lake, NM; the tuff cone was Pavant Butte, UT. The reflectance of ten to twenty powdered samples (grain size < 500 μm) from each area were analyzed in the 0.3 to 2.7-μm wavelength range at RELAB [3]. Most of the highly palagonitized tuff cone sample spectra display a 2.3-μm absorption feature; a typical Pavant Butte palagonite tuff spectrum is shown in Figure 1. The 2.3-μm feature in these samples is due to a combination of the O-H stretch and Mg-OH lattice modes [4], and is characteristic of trioctahedral Mg-bearing clay minerals. In contrast, several of the less-palagonitized tuff ring sample spectra had 2.2 μm absorption features. This indicates the presence of Al-OH bonds and is diagnostic of Al-bearing dioctahedral clay minerals. A typical tuff spectrum from the Zuni Salt Lake tuff ring is also shown in Figure 1. Note that, independent of the difference in cation between these two samples, the more heavily altered (palagonitized) tuff cone material has a much deeper band.

It should be noted that our emphasis is on the 2.2- and 2.3-μm features. These overtones are weaker than the v_{OH} stretching fundamental at 2.75μm and weaker even than the $2v_{OH}$ primary overtone at 1.38μm. However, both of the latter features are obscured by atmospheric water vapor and/or other gases in most remote sensing studies. Consequently, the 2.2- and 2.3-μm features take on a practical significance belied by their relatively shallow band depth. Details in these relatively weak features have also proven to be very diagnostic of mineralogy.

XRD analyses were performed on our samples that showed the strongest 2.2- and 2.3-μm features. XRD analyses of the initial bulk samples produced no peaks characteristic of Al-bearing clay minerals. However, the Pavant Butte samples did give a 7 Å peak that is

tentatively assigned to antigorite. The bulk samples were then broken down to sand, silt and clay sized fractions and subjected to XRD analysis in the manner of Starkey et al. [5]. Only in the clay-sized fraction of two of the three tuff-ring samples did even a weak peak in the vicinity of 15 Å appear. This is interpreted as evidence of a smectite and/or mixed layer smectite-illite.

These results demonstrate something that many planetary spectroscopists have noticed for years: reflectance spectrometry is generally a more sensitive indicator of fine-grained and/or poorly crystalline clay-type mineralogy than is the more mature technique of XRD. NIR spectrometry can detect crystalline clays even in bulk samples of poorly crystalline materials. To attempt to detect those minerals with XRD analysis requires time consuming size separation procedures. In fairness, it should also be noted that in one of the Pavant Butte samples, a 15 Å peak indicated the presence of clay minerals whereas the NIR spectrum of that same sample showed no 2.2- or 2.3-μm band. That particular sample had a low reflectance and the lack of spectral features is attributed to masking by opaque minerals. Reflectance spectrometry is not an entirely mature technique, and more attention needs to be paid to issues such as the role that opaque minerals can play in masking diagnostic absorption features. Nevertheless reflectance spectometry should continue to receive serious consideration not only for laboratory use, but for possible in-situ instrumentation on future planetary rovers.

REFERENCES: [1] Eslinger, E. and Pevear, D. (1988) *SEPM Short Course Notes* **22**. [2] Sheridan, M.F. and Wohletz, K.H. (1983) *J. Volc. Geotherm. Res.*, **17**, 1-29. [3] Pieters, C.M. (1983) *J. Geophys. Res.*, **88**, 9534-9544. [4] Hunt, G.R. and Salisbury, J.W. (1970) *Modern Geology*, **1**, 283-300. [5] Starkey, H.C. et al. (1984) *USGS Bull. 1563.*

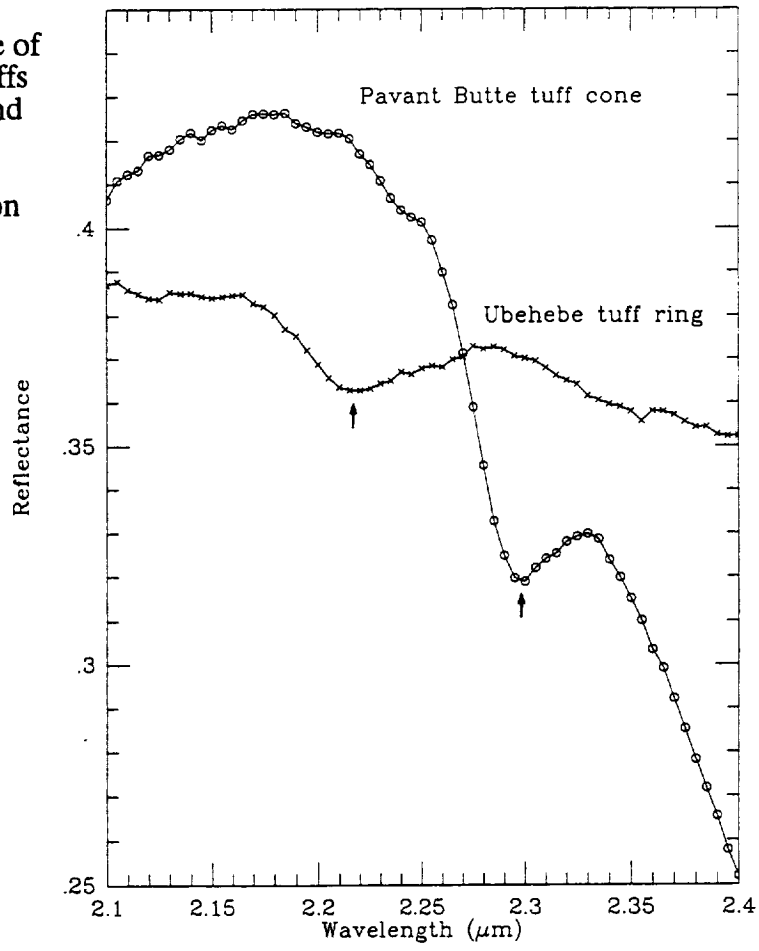

Figure 1. Near infrared reflectance of palagonitized basaltic tuffs from Ubehebe Crater and Pavant Butte. Arrows indicate the presence of 2.2 and 2.3 μm absorption features.

THERMAL NEUTRON LEAKAGE FROM MARTIAN CARBONATES.*

W.C. Feldman, Los Alamos National Laboratory, MS D438, Los Alamos, New Mexico 87545, and **B.M. Jakosky**, University of Colorado, Laboratory for Atmospheric and Space Physics and Department of Geological Sciences, Boulder, Colorado 80309

Photographic mosaics of Mars have revealed outflow channels, valley networks, and patterned ground that have been interpreted (1,2) to indicate that liquid water once flowed on Mars. The extent of these features has led many researchers to speculate (3) that surface ponds of liquid water may have been stable in early martian history, implying a thicker atmosphere and a warmer climate then than is presently observed. In fact, climatic conditions may have been sufficiently clement over a time period long enough to have supported the development of life.

If this speculation is correct, then an initially thick, predominantly carbon dioxide martian atmosphere should have been gradually transformed to carbonate rocks as the planet cooled (4). Conversely, detection of sizable carbonate deposits near the surface of Mars implies a more clement early environment and provides a focus for a search for fossil remnants of primitive life. Carbonates such as calcite ($CaCO_3$), magnesite ($MgCO_3$), dolomite ($CaMg(CO_3)_2$), and siderite ($FeCO_3$) are expected to be most abundant based on the surface composition measured using Viking instrumentation (5). However, searches for such deposits using infrared reflectance spectra have not been successful (6). Although not encouraging, these results do not imply an absence of such deposits since they would not be visible if buried under a non carbonate aeolian blanket thicker than a few microns. Such an overburden is expected to result from observed recurrent, global dust storms.

Use of neutron and gamma-ray techniques to search for substantial carbonate deposits do not suffer the foregoing limitations since neutrons and gamma rays are more penetrating than infrared photons. It is therefore reasonable to ask whether such deposits have a neutron and gamma-ray signature sufficiently distinctive to allow a unique identification. This report presents results of an initial study confined to the neutron signature of a near-surface carbonate deposit.

A previous study has shown that large, thick deposits of pure calcite and magnesite do indeed generate energy spectra of escaping neutrons that are quite distinct from that generated by regolith having the composition of Chryse Fines with one weight percent of water (7). This type of soil will be referred to simply as regolith in the rest of this report. Specifically, thermal amplitudes of upward neutron currents are increased by factors of 2.8 and 12.2 for calcite and magnesite, respectively. The same study showed no such distinctive signature for siderite because of iron's high thermal-neutron-absorption cross section. However, "global" (radii $\gtrsim$ 1000 km), thick deposits of pure calcite and magnesite are not likely on Mars. We therefore investigated the persistence of measurably enhanced thermal neutron amplitudes for three likely surface configurations. The first corresponds to the burial of a thick, global carbonate deposit under a layer of regolith. The second configuration consists of a thick, global, uniform mixture of carbonate and regolith. Such a deposit could have formed through the gardening of initially stratified layers by meteoroid bombardment or by aeolian deposition and erosion over aeons. The third configuration consists of a circular, thick, pure carbonate deposit surrounded by regolith. This case corresponds to the presence of an ancient pond of standing water that has long since evaporated.

Simulations of leakage neutron energy spectra were made for each of the three carbonate rock types that have measurable thermal amplitude enhancements – magnesite, dolomite, and calcite. In all cases, a 16 g/cm^2 atmosphere of predominantly carbon dioxide was included. Resultant thermal and epithermal amplitudes were then sorted as a function of depth of regolith overburden, in g/cm^2, in the first configuration, and in terms of percent admixture of regolith into an initially pure carbonate deposit, in the second configuration. Estimates of the detectability of surficially confined deposits were made by calculating the count rate of a neutron sensor that is similar to the Mars Observer Gamma-

MARTIAN CARBONATES USING NEUTRONS
Feldman, W. C. and Jakosky, B. M.

Ray Spectrometer (GRS) anticoincidence shield. The calculations were done assuming the hypothetical neutron sensor is orbiting Mars at the altitude of the Mars Observer, 361 km, but oriented differently than that of the GRS anticoincidence shield, for reasons of simplicity. Here we choose a detector orientation that is pointing radially downward. For this last case, count rates were sorted in terms of the diameter of pure carbonate deposit embedded within a planet-wide regolith domain.

We report only the thermal amplitude results for the first two configurations because the entire differences in epithermal amplitudes calculated between carbonate and regolith deposits reflect the selective inclusion of one weight percent of water in the regolith. This difference therefore has no bearing on the presence or absence of carbonate. In contrast, the enhancement in thermal amplitude displayed by the carbonate deposits stem from the low-to-moderate thermal neutron absorption cross sections of carbon, oxygen, magnesium, and calcium, relative to those for chlorine, titanium and iron. These last three elements are significant constituents of martian regolith.

Plots of neutron thermal amplitude against regolith overburden and percent regolith admixture show that for both, a distinctive neutron signature is detectable for significant deviations from a pure, thick carbonate deposit. Choosing as our identification criterion, a value of thermal amplitude that is 50% higher than that for a globally thick regolith deposit, these calculations indicate that 1) magnesite can be detected even if buried to depths of 59 g/cm^2 below the surface or if mixed with as much as 55 mass percent of regolith, 2) dolomite can be detected if buried to depths of 53 g/cm^2 or mixed with as much as 46 mass percent of regolith, and 3) calcite can be detected if buried to depths of 44 g/cm^2 or mixed with as much as 38 weight percent of regolith. The same identification criterion also yields detection threshold deposit diameters of 240 km for magnesite, 440 km for dolomite and 650 km for calcite.

Although the results of the first two simulations demonstrate the promise of neutrons as a sensitive probe of extensive deposits of carbonate rocks on Mars, the third simulation shows that such a search from orbit will not likely succeed. Sufficiently large diameter deposits are simply not expected. However, this impediment is removed if a search can be conducted on or near the surface such as would be possible using a low-altitude balloon or a rover.

References.
(1) Carr, M.H., *The Surface of Mars*, Yale Univ. Press, New Haven, Conn., 1981.
(2) Squyres, S.W., *Annu. Rev. Earth Planet. Sci.* **12**, 83–106, 1984.
(3) Baker, V.R., *The Channels of Mars*, Univ. Texas Press, Austin, 1982.
(4) Kahn, R., *Icarus* **62**, 175–190, 1985.
(5) Clark, B.C., A.K. Baird, R.J. Weldon, D.M. Tsusaki, L.Schnabel, and M.P. Candelaria, *J. Geophys. Res.* **87**, 10059–10067, 1982.
(6) Singer, R.B., *Adv. Space Res.* 5, 59–68, 1985.
(7) Feldman, W.C., W.V. Boynton, and D.M. Drake, in *Remote Geochemical Analysis: Elemental and Mineralogical Composition*, Pieters,C.M. and Englert,P.J., eds., LPI, Houston, in press, 1990.
* Work supported by NASA and done at Los Alamos under the auspices of the U.S. Department of Energy.

POLYPHASE NOACHIAN TECTONISM OF THE MEMNONIA/AEOLIS REGION; EVIDENCE FOR GREATER PRE-THARSIS LITHOSPHERIC MOBILITY OF MARS, Randall D. Forsythe, Dept. Geog. and Ear. Sci., UNCC, Charlotte, NC 28223 and Center for Earth and Planetary Studies, National Air and Space Museum, Smithsonian Institution, Washington D.C. 20560.

Contemporary summaries of planetary tectonics state there is no evidence of plate tectonics on Mars (1,2), no strike slip faults (3), and that a large percentage of the planets' tectonic features can be related in some fashion to the development of the Tharsis volcanic province (4,5). From this emerges the view of a Martian immobile lithosphere affected only by low strain contractional features, fractures, and graben systems. However, this view of Martian tectonics becomes much less tenable when consideration is given to a number of observations and inferences concerning Mars' ancient past(6).

Noachian lobate scarps and wrinkle ridges. The Noachian highlands of the Memnonian-Aeolis area contain an array of N to NNE trending lobate scarps that have been argued to pre-date Tharsis-centered tectonism, and which are geometrically incongruous with such an interpretation(6). More detailed mapping (7,8) using Viking imagery has confirmed that at least locally these tectonic features predate outflow channel development in Mangala Valles, and are cut by the Tharsis radial 'fracture' swarm. Kinematically, the lobate scarps have previously been interpreted as normal faults, related either to early thermal stresses(6) or to a major Noachian impact basin (8). Two observations, however, suggest that these scarps are contractional features. First, they are replaced by wrinkle ridge morphologies of similar trend where they intersect major basins, and secondly, there are abundant sharply defined linear NNW-NW and NE-NNE trending offsets of the lobate scarps and wrinkle ridges that are identical in appearance to the strike-slip faults documented in the Valles Marinaris region (9). The wrinkle ridges and inferred strike-slip faults argue for a contractional origin for the lobate scarps.

Transcurrent faults. Work in the western equatorial dichotomy boundary zone argued for the Gordii Dorsum escarpment to represent a lithospheric scale left-lateral transcurrent fault of Noachian age; perhaps indicating greater lithospheric mobility in the ancient past(10). Current analysis of the western equatorial zone has led to the discovery of an additional fault of a probable transcurrent character, here called the Apollinaris fault zone. The fault, like the Gordii Dorsum appears to have fine scale fault sculpture controlled by 2 sets of low angle oblique-trending secondary faults. Also apparent, are several oblique-trending bulges and ridges and an adjacent rhombic-shaped, and fault-limited, depression (rhomb graben?). Finally, adjacent to the rhomb 'graben' is a conspicuous array of regularly spaced assymetric warps that appear truncated and displaced in a left-lateral sense along the edges of the graben structure. The combined set of structures are restricted to what has previously been mapped as Amazonian age materials(11), but are alternatively interpreted as exhumed Noachian units(12). The combined set of structures, can be modelled an with an E-W oriented horizontal maximum compressive stress regime, with the Apollinaris fault zone (>300 km length) representing a major lithospheric-scale left-lateral shear zone like the Gordii Dorsum. Topographic profiles indicate that the NNW to NW trending transcurrent faults of this unique equatorial province (approx. 2500x500 km) parallel large scale trough/swell structures with wavelengths of 375 km and amplitudes between 1 and 3 km. To the west, south, and east highland materials in the immediate vicinity of the Apollinaris fault zone have lobate scarps and wrinkle ridges with 'strike-slip' faults of inferred left-lateral character sub-parallel to the Gordii Dorsum and Apollinaris fault zones.

Polyphase deformed Noachian 'Basement.' Finally, an analysis of the marginal Noachian zone to the south of the dichotomy boundary reveals a number of lines of evidence for erosional resurfacing of a previously deformed(polyphase) basement complex. Here erosional resurfacing in the intercrater plains has etched the surface traces of cross-cutting linear and curvi-linear penetrative fabrics. The fabrics (typically with NW and NE sets represented) have controlled crater basin shapes likely by a combination of primary syncratering excavation, the secondary post-excavation collapse of crater walls, and by later tertiary erosional processes. The fabrics have also controlled dendritic tributary systems within the Noachian intercrater plain areas, as well as the development of outflow channels near the dichotomy boundary. Large craters near the dichotomy boundary reveal internal walls with at least two orientations of fabrics that are seen penetrating at least to the base of crater walls with >1 km relief. Do the fabrics represent bedding, cleavages, or foliations? In one outflow channel (Viking 443S13) erosion reveals the edges of a series of resistant west dipping layers.

Viewed collectively the Noachian data set argues for at least two, if not three, phases of regional tectonism prior to Tharsis development. Penetrative fabrics and upturned layers, appear to be regionally present but largely masked by the highland 'regolith'. Where exposed, however, they provide tantalizing opportunities to gain a glimpse of what appears to be a very different, and more tectonically active phase of Mars' history. The N-S lobate scarps and NW trending transcurrent faults were superimposed on this polyphase deformed basement probably during the late Noachian. Preliminary analysis suggests E-W shortening strains >7.5 % that affected an area >3000 km x 1500 km. This appear larger than that inferred for the circum-Tharsis ridge structures(12) and may reflect a trend towards increasing stabilization (13).

Photomosaic of the Apollinaris Patera region (7S,187W; Approx. scale: 1cm=37 km) AP: Caldera wall of Apollinaris Patera, AF: Apollinaris fault zone (inferred left-lateral transcurrent fault), RG: rhomb 'graben', NAW: northern array of asymmetric 'warps' in the Medusa Fossa Fm., SAW: southern area of warps in the Medusa Fossa Fm., sf: NW-trending offsets of lobate scarps (small strike-slip faults).

REFERENCES (1) Basaltic Volcanism Study Project (1981) Volc. of the Terr. Planets (Pergamon, N.Y.) (2) Carr, M.H. et al. (1984) Geology of the Terrestrial Planets, NASA SP-469, 317 (3) Carr, M.H. (1981) The Surface of Mars, Yale Univ. Press, 232 (4) Wise, D.U., Golombek, M.P. & McGill, G.E. (1979) Icarus 38, 456-472 (5) Phillips, R.J. & Ivins, E.R. (1979) Phys. Earth planet. Inter. 19, 107-148 (6) Schultz, R.A. (1985) JGR 90, 7849-7860 (7) Craddock,R., Zimbelman, J.R., & Watters, T.R. (1989) LPI Tech. Rpt. 89-06, 18-20 (8) Craddock, R. & Zimbelman J.R. (this volume) (9) Schultz, R.A. (1989) Nature 341, 424-425 (10) Forsythe, R.D. & Zimbelman, J.R. (1988) Nature 336, 143-146 (10) Morris, E.C. & Dwornik, S.E. (1978) USGS Map I-1049 (11) Forsythe, R.D. & Zimbelman, J.R. (this volume) (12) Watters, T.R. (1988) JGR 93, 10236-10254.

A DISCUSSION OF MARS' WESTERN EQUATORIAL DICHOTOMY BOUNDARY ZONE; ENIGMAS, ANOMALIES AND CONTROVERSIES, Randall D. Forsythe, UNCC, Charlotte, NC 28223, and James R. Zimbelman, Center for Earth and Planetary Studies, National Air and Space Museum, Smithonian Institution Washington, D.C. 20560.

Mars' equatorial region from the western edge of the Tharsis volcanic province (approx. 135 Long.) west to Apollinaris Patera (approx. 186 Long.) is a transitional realm lying at elevations between 0 and 3000 meters that separates young, low lying, deposits of the northern hemispheres' plains, from high and old intensely cratered materials of the southern hemisphere (1). The region, which corresponds to the classical high albedo areas of Zephria and Mesogaea contains deposits of unusual morphologic, structural, and geophysical characteristics.

A morphologic enigma: Following Mariner 9 data analysis the unusual deposits of the area were characterized as rolling or undulating plains of 'layered' and/or lineated deposits that were suggested to be a succession of lava flows younger than the highlands to the south(2). Viking images permitted detailed mapping, defining a number of units within what has been called the Medusa Fossa Formation(3), and led to a suggestion that they may represent a unique sequence of ignimbrite and tuffaceous units(4,5). A recent interpretation, based on a comparison to layered deposits of similar morphological character surrounding Mars' residual ice caps has led to the suggestion that they may represent an eastward younging track of paleopole deposits, begging the corollary of Martian polar wander(6).

A structural anomaly: Maps of the Zephyria and Mesogaea region show a number of NW to NNW trending structural elements within the layered and lineated deposits that are defined as linear depressions, grabens, or scarps(3). One of these, the Gordii Dorsum, has been recently argued to represent a major left-lateral transcurrent shear zone within the Martian lithosphere(7). Our analysis of Viking imagery reveals similar secondary structures along an equally pronounced NW trending fault zone at the extreme western edge of the belt, that runs along the northern base of Apollinaris Patera. This zone is tracable for some 300 kilometers; diagonally cutting across the transitional province to NW where it disappears under undeformed cover of Elysium Planitia. The Gordii Dorsum and the Apollinaris fault bracket on the east and west sides, respectively, a province that stretches for a minimum 2300 kilometers and appear divisible into 5 to 7 major NW-NNW trending trough/swell couplets with an average wavelength of 375 km and amplitudes of 1 to 3 kilometers. From Gordii Dorsum in the east to Apollinaris Patera in the west there is also a gradual counterclockwise shift of 15 to 20 degrees from NNW to NW orientations, which is opposite that expected from Tharsis models.

An age paradox: While early mapping efforts mapped the transition or dichotomy boundary zone in this region as having materials of intermediate (Hesperian) ages(2), subsequent revisions reversed stratigraphic relations between deposits of this zone and the northern plains materials(3), making them Amazonian. The hypothesis of a layered track of paleopole deposits accepted Amazonian chronologies but argued for an east to west younging pattern(6). The structural arguments paradoxically contradict the relative ages suggested by crater statistics, and would require yet a third revision in the relative age of the province as a whole with respect to surrounding terranes. However, an analysis of crater statistics in the boundary zone to the west (8), as well as our analysis of crater statistics in the this transitional region indicated extensive resurfacing. Cumulative crater frequency v.s. log diameter curves for 200,000 sq km windows of high and low topographic regions of the transition zone suggest a positive correlation of resurfacing effects with topography, not

easily modelled with the ignimbrite or paleopole deposit hypotheses.

Evidence for extensive erosion: Erosional processes that have operating in the dichotomy boundary zone include wind, mass wasting, surface runoff, and possible karst. The minimum depths of erosion are calculated from preserved erosional features in the zone, along the margin with the highlands to the south, and from features within the highlands but still within the marginal region where crater statisical analysis and morphologies document the north to south retreat of the dichotomy boundary. Within the zone mesas, cuestas, and pedestal craters document erosional down-cutting up to 1.1 km; cliffs and canyon walls, along the boundary, document an erosional base level approximately 1 kilometer below perched intercrater plains. Retreat of the highlands from north to south is further supported by the tracing of intrahighlands structural fabrics across the boundary into the transitional province.

Radar & thermal imaging: Thermal inertia of the region is low (9) and is equivalent to an average particle size of >40um for an assumed homogeneous particle surface of one particle size (10). Materials with this value of thermal inertia will completely mask any underlying material (including solid bedrock) if the layer is >2 cm thick on the surface. 3.5 cm radar measurements made during the 88 Mars opposition showed zero depolarized radar echo power in the equatorial region to the west of Tharsis, and strong echo power in the volcanic provinces surrounding the region to its south and east (11). Cursory inspection of a published version of the synthetic radar imaging centered along the 133 and 147 meridian shows an apparent correlation with the transitional zone along the dichotomy boundary(12). Also noted here were discernable echoes from the region surrounding the residual southern polar ice cap, where the modern day equivalent of the postulated paleopole deposits are found. Echo power in the RCP transmitted/LCP received signal is due to multiple surface reflections or multiple subsurface scatterers, and for the equatorial deposits has been interpreted (accommodating thermal data) as an area of fine grained deposits with the absence of volume scatterers to a depth of several meters(11).

A chemical boundary layer hypothesis: An alternative interpretation which may accommodate the combined set of observations (structural, morphologic, crater statistics, and geophysical data) is that the western equatorial region represents an elogate (2-3000 km), 300-500km wide, arch of previously deformed and cratered material that sat initially in excess of 1 to 1.5 km depth beneath the cratered highlands. Exhumation and erosional retreat of the dichotomy boundary brought the earlier intra-highlands erosional base level (?water table) with its attended salt-cemented formations to the surface. The chemical processes attendent with the paleowater table gives a mechanism for masking large craters, the formation of the apparent molds of barchan dunes(13), and explaining crypic cross-cutting layering in the 'layered' sequences. Like the salt-cemented ranges of the Atacama Salar (Chile)(14) uplift initiates a process of decementation leaving an upper fine grained residual layer upwards of 2 meters thick. Such a decemented layer would explain the concurrence of the radar "stealth" zone and low thermal inertias with the exhumed basement arch.

References: (1) Scott, D.H. & Carr, M.H. (1978) USGS Map I-1083 (2) Morris, E.C. & Dwornik, S.E.(1978) USGS Map I-1049 (3) Scott, D.H. & Tanaka, K.L.(1986) USGS Map I-1802A (4) Scott, D.H. & Tanaka, K.L.(1982) JGR 87,1179-1190 (5) Scott, D.H. & Tanaka, K.L.(1981) USGS I-1280 (6) Schultz, P.H. & Lutz, A.B. (1988) Icarus 73, 91-141 (7) Forsythe, R.D. & Zimbelman, J.R.(1988) Nature 336, 143-146 (8) Craddock, R.B. & Maxwell, T.A. (1989) LPSC XX, 191-192 (9) Kieffer, H.H., et al. (1977) JGR 82, 4249-4291 (10 Kieffer, H.H., et al. (1973) JGR 84, 8252- 8262 (11) Butler, B., et al. (1989) EOS 70, 1171 (12) Anonymous (1989) Astronomy 17, 12 (13) Rhodes, D.D. & Neal, T. (1981) NASA Tech. Mem. 84211, 232-234 (14) Stoertz, G.E. & Ericksen, G.E. (1974) USGS Prof. Paper 811